POLITECNICO DI TORINO
Repository ISTITUZIONALE

Multiscale agent-based modeling of restenosis after percutaneous transluminal angioplasty: Effects of tissue damage and hemodynamics on cellular activity

(Article begins on next page)

28 April 2024

Multiscale agent-based modeling of restenosis after percutaneous transluminal angioplasty: effects of tissue damage and hemodynamics on cellular activity

Anna Corti[1], Monika Colombo[1,2], Francesco Migliavacca[1], Scott A. Berceli[3,4], Stefano Casarin[5,6,7], Jose F. Rodriguez Matas[1], Claudio Chiastra[1,8,*]

1. Laboratory of Biological Structure Mechanics (LaBS), Department of Chemistry, Materials and Chemical Engineering "Giulio Natta", Politecnico di Milano, Milan, Italy
2. Institute for Chemical and Bioengineering, Department of Chemistry and Applied Biosciences, ETH Zürich, Switzerland
3. Department of Surgery, University of Florida, Gainesville, FL, USA
4. Malcom Randall VAMC, Gainesville, FL, USA
5. Department of Surgery, Houston Methodist Hospital, Houston, TX, USA
6. Center for Computational Surgery, Houston Methodist Research Institute, Houston, TX, USA
7. Houston Methodist Academic Institute, Houston, TX, USA
8. PoliTo[BIO]Med Lab, Department of Mechanical and Aerospace Engineering, Politecnico di Torino, Turin, Italy

*Address for correspondence:

Claudio Chiastra, PhD

PoliTo[BIO]Med Lab

Department of Mechanical and Aerospace Engineering

Politecnico di Torino

Corso Duca degli Abruzzi, 24

10129 Turin, Italy

ORCID: 0000-0003-2070-6142

E-mail: claudio.chiastra@polito.it

Abstract

Background. Restenosis following percutaneous transluminal angioplasty (PTA) in femoral arteries is a major cause of failure of the revascularization procedure. The arterial wall response to PTA is driven by multifactorial, multiscale processes, whose complete understanding is lacking. Multiscale agent-based modeling frameworks, simulating the network of mechanobiological events at cell-tissue scale, can contribute to decipher the pathological pathways of restenosis. In this context, the present study proposes a fully-automated multiscale agent-based modeling framework simulating the arterial wall remodeling due to the wall damage provoked by PTA and to the altered hemodynamics in the post-operative months.

Methods. The framework, applied to an idealized femoral artery model, integrated: (i) a PTA module (i.e., structural mechanics simulation) computing the post-PTA arterial morphology and the PTA-induced damage, (ii) a hemodynamics module (i.e., computational fluid dynamics simulations) quantifying the near-wall hemodynamics, and (iii) a tissue remodeling module simulating cellular activities through an agent-based model.

Results. The framework was able to capture relevant features of the 3-month arterial wall response to PTA, namely (i) the impact of the PTA-induced damage and altered hemodynamics on arterial wall remodeling, including the local intimal growth at the most susceptible regions (i.e., elevated damage levels and low wall shear stress), (ii) the lumen area temporal trend resulting from the interaction of the two inputs, and (iii) a 3-month lumen area restenosis of ~25%, in accordance with clinical evidence.

Conclusions. The overall results demonstrated the framework potentiality in capturing mechanobiological processes underlying restenosis, thus fostering future application to patient-specific scenarios.

Keywords

Percutaneous transluminal angioplasty (PTA), restenosis, arterial wall remodeling, femoral artery, mechanobiology, systems biology, multiscale modeling, agent-based modeling (ABM), finite element analysis, computational fluid dynamics

1. Introduction

Peripheral artery disease (PAD) is an occlusive pathology affecting more than 230 million adults worldwide (a global prevalence of ~ 5.6%) (Criqui et al., 2021). The lower limb arteries, and in particular the superficial femoral artery (SFA), are among the vessels most affected by PAD (Kasapis and Gurm, 2010). The choice of the optimal endovascular treatment for PAD in SFA is still controversial and can depend on the lesion characteristics, such as the length, location, and plaque composition (Tepe et al., 2015). Although percutaneous transluminal angioplasty (PTA) is widely adopted as primary endovascular procedure in SFA, it suffers from a ~60% 1-year primary patency rate, mainly due to neointimal hyperplasia and subsequent restenosis (Katsanos et al., 2014). The endothelial denudation and arterial wall damage induced by balloon expansion is thought to be the primary trigger of neointimal hyperplasia through the activation of an inflammatory cascade promoting exacerbated cellular activity and ultimately leading to excessive tissue re-growth and potential restenosis (Parmar et al., 2009; Schillinger and Minar, 2005; Toutouzas et al., 2004). Moreover, the post-intervention hemodynamics alteration contributes to the arterial wall remodeling through a direct or endothelial-mediated effect on vascular cell dynamics (Chistiakov et al., 2017; Harrison et al., 2006; Koskinas et al., 2012). Despite the extensive in-vitro, in-vivo and in-silico research aimed at deciphering the underlying mechanisms of restenosis following PTA, a complete understanding of the mechanobiological processes of this adverse tissue response is still lacking.

The development of in-silico frameworks coupling continuum- and agent-based models (i.e., multiscale agent-based modeling frameworks) has emerged as a promising approach for the investigation of vascular adaptation processes, well capturing the intrinsic multiscale, multifactorial and interconnected events in a systems biology perspective (Corti et al., 2021). To date, several multiscale agent-based modeling frameworks of arterial wall remodeling after endovascular procedure have been proposed (Corti et al., 2021). However, they were mainly focused on either the

wall damage- or the hemodynamic-related factors promoting restenosis (Boyle et al., 2011, 2010; Caiazzo et al., 2011; Li et al., 2019; Nolan and Lally, 2018; Tahir et al., 2014, 2013, 2011; Zahedmanesh et al., 2014; Zun et al., 2017, 2019). The present study proposes a fully-automated multiscale agent-based modeling framework simulating the arterial wall remodeling due to both the wall damage provoked by PTA and the altered hemodynamics in the post-operative months. The framework integrates: (i) a structural mechanics simulation of PTA in a diseased femoral artery model to compute the arterial wall damage, (ii) computational fluid dynamics (CFD) simulations in the post-intervention artery model to quantify the near-wall hemodynamics, and (iii) an agent-based model (ABM) of arterial wall remodeling to simulate the cellular activity in response to the computed arterial wall damage and near-wall hemodynamics.

First, to assess the ABM working mechanisms and verify the correctness of the model formulation, the ABM of arterial wall remodeling was tested under idealized scenarios. Then, the entire framework (PTA simulation and CFD simulations coupled with the ABM) was applied to an idealized diseased SFA model simulating the arterial response along a follow-up period of 3 months.

2. Methods

2.1. Multiscale framework

Figure 1 shows the multiscale framework of restenosis following PTA. The framework receives as input the geometry of the diseased SFA artery, performs the structural mechanics simulation of the PTA procedure (PTA module), executes the CFD simulation in the post-PTA artery model (hemodynamics module), simulates the post-intervention arterial wall remodeling through the agent-based modeling approach and reconstructs the new SFA geometry at prescribed follow-ups (tissue remodeling module). Within the PTA module, the geometry of the three-dimensional (3D) diseased SFA is meshed and a structural mechanics simulation of balloon

expansion solved through the finite element method is performed. The arterial wall damage induced by the intervention procedure is quantified within the intima layer and used as input to the tissue remodeling module. The lumen surface of the deformed vessel configuration resulting from the PTA simulation is given as input to the hemodynamics module for the computation of the post-intervention hemodynamics. The fluid domain of the 3D post-PTA SFA model is meshed, a steady-state finite volume CFD simulation is performed, and the computed wall shear stress (WSS) profiles are extracted at selected bidimensional (2D) cross-sections and used to initialize the tissue remodeling module. Within the tissue remodeling module, a 2D ABM, implemented for each vessel cross-section, simulates the post-intervention arterial wall remodeling in response to the PTA-induced damage and the near-wall hemodynamics, by replicating cellular and extracellular matrix (ECM) dynamics. At a predefined coupling period (1 month in the present study), the ABM simulations are interrupted, the lumen surface of the SFA model is reconstructed from the ABM outputs and the hemodynamics module – tissue remodeling module sequence is repeated to compute the hemodynamics in the current remodeled arterial geometry and consequently update the ABM hemodynamic stimulus to the cellular activities. This sub-cycle is performed until a desired follow-up time (3 months in the present study). The framework is fully automated and executed through an external subroutine in Matlab (MathWorks, Natick, MA, USA).
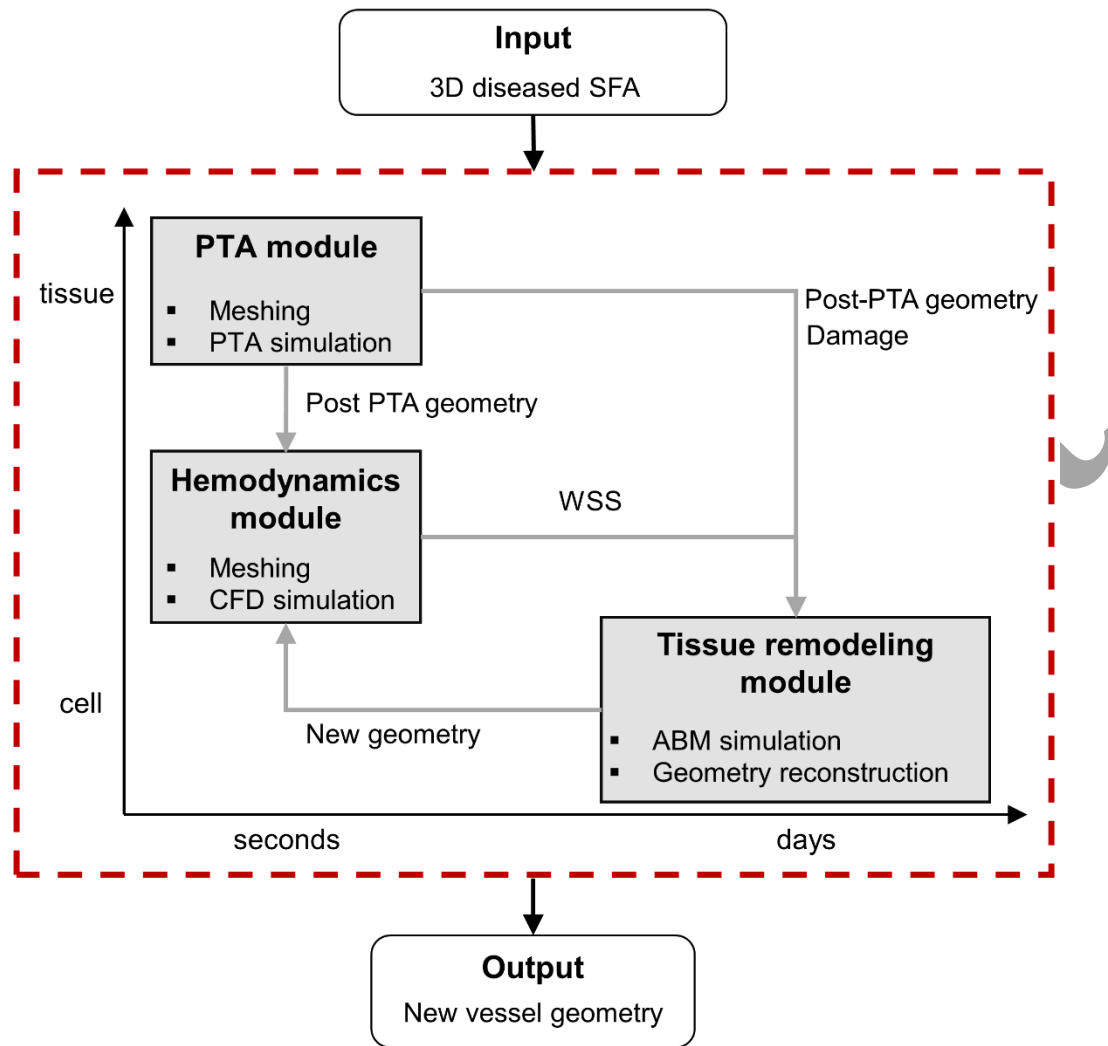
Figure 1. Multiscale computational framework. Starting from the diseased superficial femoral artery (SFA) model, the framework (dashed red box) simulates: (i) the percutaneous transluminal angioplasty (PTA) procedure (PTA module) at the tissue-seconds scale, through a structural mechanics simulation solved by means of the finite element method, (ii) the post-intervention hemodynamics (hemodynamics module) at the tissue-second scale, through finite volume computational fluid dynamics (CFD) simulations, and (iii) the post-intervention arterial wall remodeling along 3 simulated months (tissue remodeling module) at the cell-days scale, through a bidimensional (2D) agent-based model (ABM). Finally, from the ABM outputs, a new three-dimensional (3D) vessel geometry is reconstructed.

2.1.1. 3D SFA model

An idealized 3D model of diseased SFA, presenting with an eccentric plaque, was generated using Rhinoceros (Robert McNeel & Associates, Seattle, WA, USA) (Fig. 2A). The dimensions of

the healthy portion of the SFA model were based on human femoral artery data. In particular, the healthy lumen diameter was set to 6.5 mm (Liang, 2020; Wood et al., 2006) while the ratios reported in Table 1 were adopted to define the intima, media and adventitia thickness (Hafner et al., 2016; Wong et al., 1993). The atherosclerotic region was built assuming a percentage area stenosis of ~65% (moderate stenosis) and an outward enlargement according to Glagov's phenomenon (Glagov et al., 1987). The outward expansion of the intima layer was assumed to compensate the initial plaque growth until the area occupied by the lesion was ~20% of the healthy lumen area (Fok, 2016). Specifically, the geometry construction consisted of a 2-step process. First, the diameter of the internal elastic lamina was enlarged (i.e., outward intimal growth) while preserving the lumen diameter as well as the healthy media and adventitia thicknesses. This produced an enlargement of the external diameter. Then, the lumen diameter was reduced to generate a 65% stenosis on the lumen area. The resulting dimensions of the SFA model are summarized in Table 2.
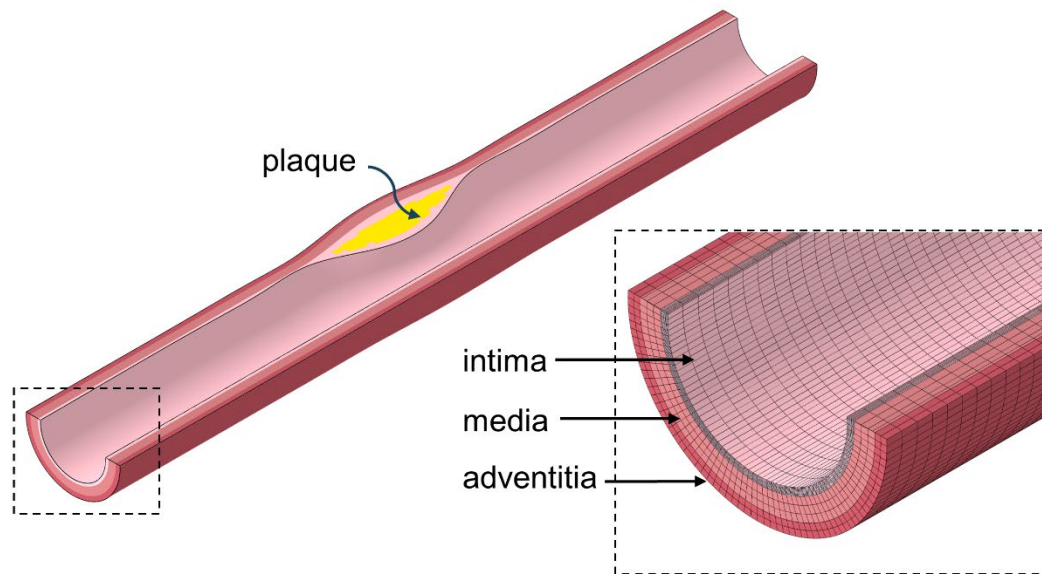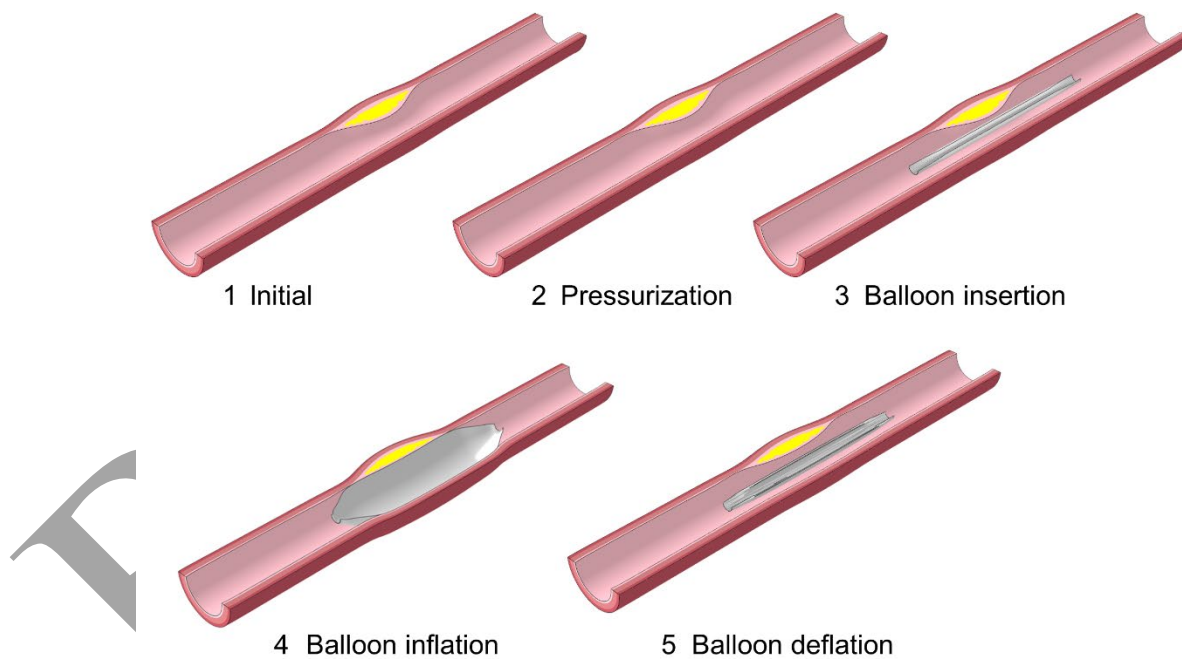
Figure 2. A) Three-dimensional model of diseased superficial femoral artery, with a detail on the mesh (dashed box).

B) Percutaneous transluminal angioplasty (PTA) simulation: 1. Initial configuration; 2. Pressurization at 100 mmHg; 3.

Balloon insertion; 4. Balloon inflation at 15 atm and 5. Balloon deflation.

Table 1. Arterial wall dimensions

Dimension [Reference]	Value	Region
Wall thickness / Lumen diameter (Hafner et al., 2016)	0.22	Human popliteal artery
Intima thickness / Wall thickness (Wong et al., 1993)	0.18	Human common femoral artery
Media thickness / Wall thickness (Wong et al., 1993)	0.52	Human common femoral artery
Adventitia thickness / Wall thickness (Wong et al., 1993)	0.30	Human common femoral artery

Table 2. Dimensions of the idealized three-dimensional superficial femoral artery model. The diseased diameters are related to the most stenotic vessel cross-section (central cross-section).

Entity	Value [mm]
Total length	70
Healthy lumen diameter	6.5
Healthy external diameter	9.4
Diseased lumen diameter	3.8
Diseased external diameter	10.2

2.1.2. PTA module

SFA model

The arterial wall was meshed with ~450,000 eight-node brick elements with reduced integration using HyperMesh (Altair Engineering, Troy, MI, USA) (Fig. 2A). Isotropic hyperelastic constitutive models were implemented to describe the mechanical properties of the healthy, diseased and plaque arterial wall tissues. The intima, media and adventitia layers of the healthy ends were assumed as almost incompressible (Poisson's ratio of 0.495) and modeled through a second-order polynomial strain energy function (Prendergast et al., 2003), as follows:

$$U = \sum_{i+j=1}^{2} C_{ij} (\bar{I}_1 - 3)^i (\bar{I}_2 - 3)^j + \sum_{i=1}^{2} \frac{1}{D_i} (J^{el} - 1)^{2i} \qquad (1)$$

10

where C_{ij} and D_i are material parameters, $\bar{I}_1$ and $\bar{I}_2$ are the first and second invariants of the deviatoric right Cauchy-Green deformation tensor and J^{el} is the elastic volume ratio. Perfect plasticity was imposed to simulate tissue failure at a Cauchy stress of 0.2 MPa (Kamenskiy et al., 2015), in agreement with the strategy proposed in previous finite element structural analyses of endovascular procedures (Gökgöl et al., 2017; Iannaccone et al., 2017). The material parameters were derived from experimental data on human femoral arteries (Prendergast et al., 2003) and are summarized in Table 3. The intima in the diseased portion was modeled as a highly calcified tissue through a neo-Hookean strain energy function with material parameters calibrated from experimental data on human atherosclerotic femoral plaques (Cunnane et al., 2015), detailed in Table 3. Moreover, the ductile damage model available in Abaqus (Dassault Systèmes Simulia Corp., Johnston, RI, USA) was adopted to describe the progressive softening behavior of the intima material (in the diseased portion) under stretch and compute for each element an associated level of damage, which will be then used as input for the subsequent ABM simulation (see Section 2.1.4). Specifically, the damage model (Smith, 2009) was set to obtain a damage initiation in correspondence with a Cauchy stress of 0.1 MPa (Cunnane et al., 2015) and an exponential evolution. Finally, the calcified plaque material was described by coupling an Ogden strain energy function, as follows:

$$U = \sum_{i=1}^{3} \frac{2\mu_i}{\alpha_i^2} (\bar{\lambda}_1^{\alpha_i} + \bar{\lambda}_2^{\alpha_i} + \bar{\lambda}_3^{\alpha_i} - 3) + \sum_{i=1}^{3} \frac{1}{D_i} (J^{el} - 1)^{2i} \qquad (2)$$

where μ_i, α_i and D_i are temperature-dependent material parameters, and $\bar{\lambda}_i$ are the deviatoric principal stretches. A perfect plasticity model was considered to mimic plaque failure at a Cauchy stress of 0.2 MPa (Loree et al., 1994), as proposed by (Chiastra et al., 2016b; Gökgöl et al., 2017; Iannaccone et al., 2017). The calcium material parameters were derived from experimental tests on human atherosclerotic plaques (Loree et al., 1994) and are reported in Table 4. The density of the arterial tissue materials was set to 1000 kg/m³.

11

Table 3. Material parameters of the intima, media and adventitia layers of the healthy extremities (healthy artery) and of the intima in the diseased portion (diseased intima).

Parameter	C_{10} [MPa]	C_{01} [MPa]	C_{20} [MPa]	C_{11} [MPa]	C_{02} [MPa]	D_1	D_2
Healthy artery	0.0189	0.00275	0.59042	0.85718	0	0.46189	0.175
Diseased intima	0.0341	0	0	0	0	0.88754	0

Table 4. Material parameters of the calcified plaque.

Parameter	μ_1	α_1	μ_2	α_2	μ_3	α_3	D_1	D_2	D_3
Value	-83.08473	2.000048	54.08689	4.000048	29.04662	-1.999967	0.41	0	0

In order to replicate the tissue environment surrounding the SFA in-vivo, a 5.5 mm thick layer surrounding the vessel model was created. The surrounding layer was meshed with ~23,000 8-node brick elements with reduced integration in Hypermesh. Its material was described as a isotropic linear elastic constitutive law with properties coherent with those of a skeletal muscle (Sierra et al., 2015) and a density of 1000 kg/m^3.

Balloon model

The model of the Armada 35 PTA balloon (Abbott Laboratories, Abbott Park, IL, USA) was created using SolidWorks (Dassault Systèmes, SolidWorks Corp., Waltham, MA, USA) in its crimped configuration, with a length of 20.0 mm and a nominal diameter of 7.0 mm. The balloon geometry was represented as a multi-wing structure (Antonini et al., 2021; Chiastra et al., 2018; Grundeken et al., 2018). The balloon thickness was set to 0.025 mm (Chiastra et al., 2018). The balloon geometry was discretized with ~16,000 reduced integration membrane elements in HyperMesh. The polymeric material of the balloon was modeled through a linear elastic isotropic model (Chiastra et al., 2018) with Poisson's ratio of 0.45 and Young's modulus of 1.15 GPa,

obtained after a calibration procedure on the pressure-diameter curve provided by the manufacturer. The material density was set to 1000 kg/m^3 (Chiastra et al., 2018).

PTA simulation

The PTA procedure was simulated through the following steps using the finite element solver Abaqus/Explicit (Fig. 2B): (i) initial undeformed configuration, (ii) pressurization of the SFA model, through the imposition of a uniform pressure of 100 mmHg to the internal surface of the vessel (this load was maintained throughout the entire simulation), (iii) balloon positioning, (iv) balloon inflation, by applying a uniform pressure of 15 atm to the internal surface of the balloon, and (v) balloon deflation, by applying a negative uniform pressure of 0.15 atm to the internal surface of the balloon. Each procedural step was simulated as quasi-static processes, as discussed elsewhere (Chiastra et al., 2018). Interactions between the balloon, the SFA model and the layer surrounding the vessel were defined through the general contact algorithm, setting a 'hard' normal behavior and a tangential behavior with friction coefficient of 0.2 (Chiastra et al., 2018). As boundary conditions, no motion was allowed to the nodes of the vessel extremities and to the nodes of the external surface of the surrounding layer. At the proximal end, only the balloon radial displacement was allowed, while at the distal end only the balloon axial translation was constrained.

As simulation output, from the deformed SFA configuration at step (v), the lumen surface was exported for the subsequent CFD simulation (Section 2.1.3). The nodal coordinates of the entire geometry together with the associated damage variable were used as input for the ABM, as detailed in Section 2.1.4.

2.1.3. Hemodynamics module

The luminal surface of the deformed SFA model obtained at the end of step (v) of the PTA simulation (Fig. 2B) was extracted and used to compute the post-intervention hemodynamics (Fig. 3). The fluid domain was meshed in Fluent (Ansys Inc., Canonsburg, PA, USA) with polyhedral elements and five layers of prism elements near the wall. A curvature-based refinement criterion

13

was adopted to accurately capture the geometrical features. The optimal mesh (~300,000 elements) in terms of both the hemodynamic output and ABM generation was identified through a mesh sensitivity analysis. A steady-state CFD simulation was performed using the finite volume-based solver Fluent, by imposing a parabolic velocity profile (mean velocity of 0.08 m/s, corresponding to a flow-rate of 200 mL/min (Holland et al., 1998; Klein et al., 2003)) at the inlet, zero pressure at the outlet, and the no-slip condition at the rigid walls. The blood was modeled as a non-Newtonian Carreau fluid with a density of 1060 kg/m^3 (Chiastra et al., 2016a). Details about the solver settings are reported in Table 5. The WSS profiles were extracted at 19 evenly-spaced (3 mm) cross-sectional planes (Fig. 3) and passed to the tissue remodeling module to perform the subsequent ABM analysis.
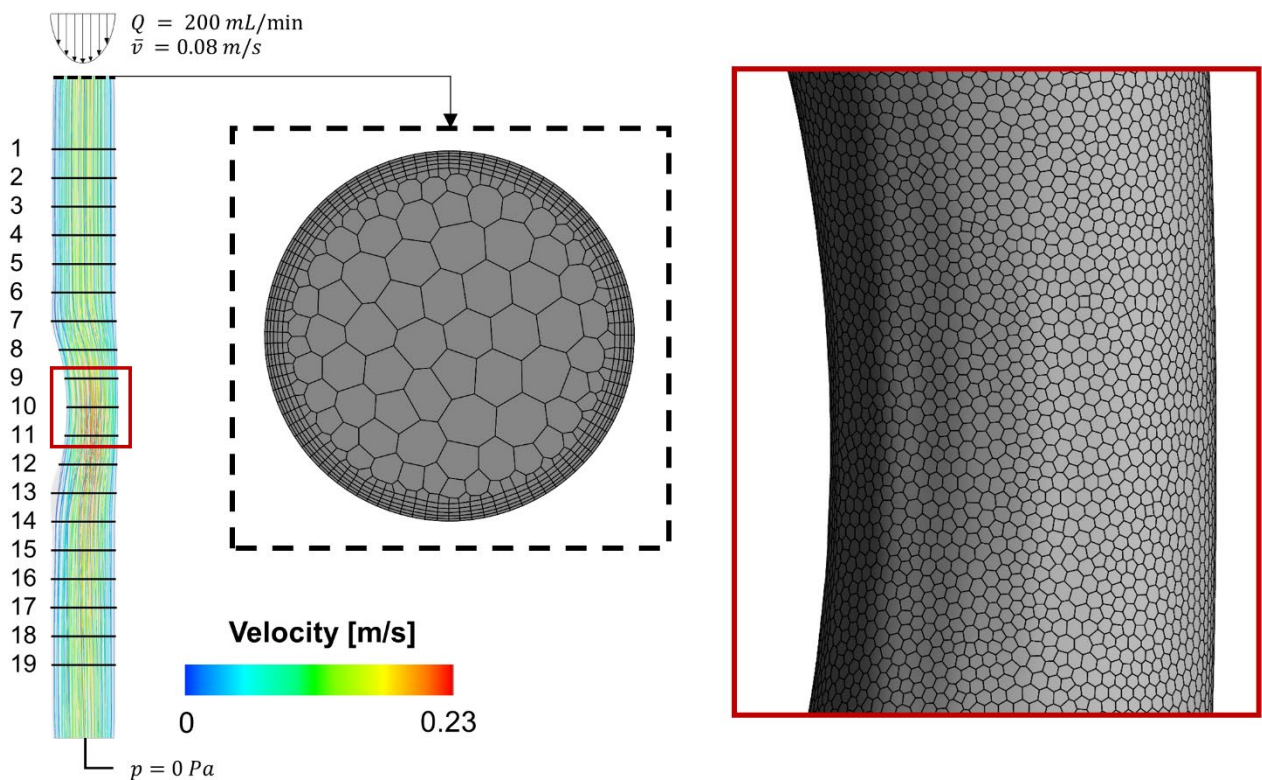

Figure 3. Hemodynamics module. The velocity streamlines obtained from the computational fluid dynamics (CFD) simulation in the deformed superficial femoral artery model are shown. The 19 cross-sectional planes selected for the subsequent agent-based model analysis are displayed on the lumen surface. Details of the polyhedral CFD mesh of the inlet and wall portion are shown in the dashed black box and in the red box, respectively.

Table 5. List of the CFD solver settings

Type	Ansys Fluent – pressure-based
Pressure-velocity coupling method	Coupled
Spatial discretization scheme–gradient	Least squares cell based
Spatial discretization scheme–pressure	Second order
Spatial discretization scheme–momentum	Second order upwind
Convergence criterion for the global residuals	5×10^{-5}

2.1.4. Tissue remodeling module

A 2D ABM at the cell-tissue scale was implemented in Matlab for each of the 19 selected vessel cross-sections to simulate the pathophysiological arterial wall remodeling in response to the PTA-induced wall damage and near-wall hemodynamics (Fig. 4). The formulation of the ABM of restenosis was based on previously developed ABMs of atherosclerosis and in-stent restenosis (Corti et al., 2022, 2020, 2019), which were here adapted according to the different simulated scenario and underlying hypotheses through the definition of suitable inputs, probabilistic rules and regularization processes, as detailed below.

The 2D ABM was implemented on a 300×300 hexagonal grid and was generated by importing, scaling, rotating and translating the nodal 3D coordinates from the deformed SFA geometry (step v on Fig. 2B), at the axial coordinate corresponding to the 19 selected cross-sections. Considering the smooth muscle cell (SMC) diameter ~25 μm (Tahir et al., 2015), a scale factor of 0.0375 mm/ABM site was adopted, thus assuming 1.5 cells per ABM site. Moreover, a three-layered arterial wall ABM structure was obtained by following the node-layer association of the SFA model of the PTA module. Each layer (i.e., intima, media and adventitia) was populated with proper cell and ECM agents, namely SMCs, collagen and elastin in the intima and media layers, and fibroblast and collagen in the adventitia. As defined in (Corti et al., 2020), a SMC/ECM

15

ratio of 0.72 (Vermeulen et al., 2001) and a collage/elastin ratio of 0.63 (Sindram et al., 2011) were initially set in the intima and media layers, respectively, while a fibroblast/collagen ratio of 0.43 was initially prescribed in the adventitia layer (Sokolis, 2008).
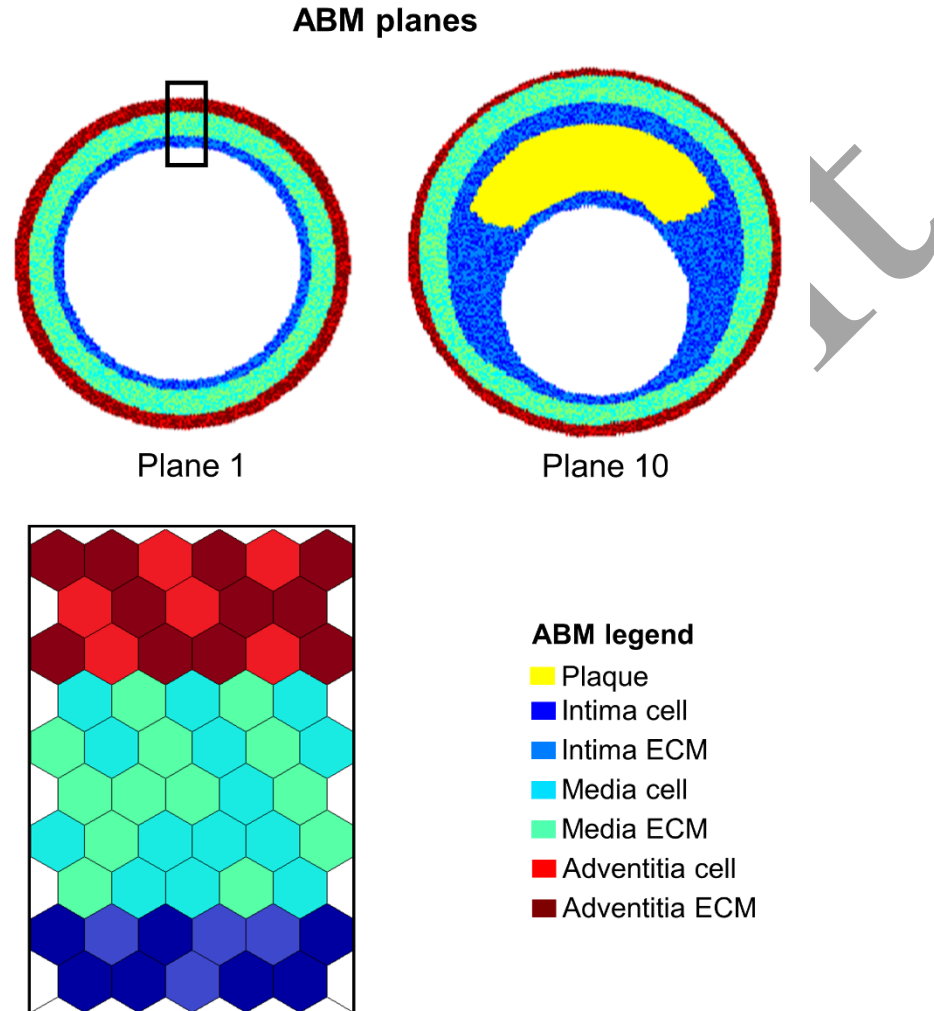
ABM planes

Figure 4. Agent-based model (ABM) of plane 1 and plane 10 (Fig. 3) and detail on the hexagonal grid.

The ABM was then initialized with the damage- and WSS-based inputs (*Dinput* and *WSSinput*, respectively), computed through the structural mechanics simulation of PTA and post-intervention CFD simulation, respectively. Regarding *Dinput*, each agent in the intima was initialized either with the associated level of damage, as computed by the PTA simulation, in the atherosclerotic region (i.e., the only portion for which the damage model was considered) or with a null damage elsewhere (i.e., at the cross-sections of the healthy portions). Being the PTA-induced

16

injury considered as one of the main triggering event for the post-intervention inflammatory response (Schillinger and Minar, 2005), it was assumed that regions presenting with higher levels of damage were associated with an augmented inflammatory response, and subsequent cellular activation and restenosis than elsewhere. Accordingly, the agent-specific level of damage was used as local weight of a generic post-intervention inflammatory curve (Edelman and Rogers, 1998) (Fig. 5), characterized by an early peak, followed by a rapid and then slow decay until 1 month after the intervention. Moreover, in accordance with previous findings (Jiang et al., 2004), the presence of a 3-day delay between the cellular activation and the inflammatory stimulus was hypothesized. For each agent k, the *Dinput* was thus defined as:

$$Dinput(t)^k = \ damage^k \times Inflammation(t - delay) \qquad (3)$$

where $damage^k$ is the agent-specific level of damage derived from the PTA simulation and $Inflammation(t - delay)$ is the generic inflammatory curve, translated to reproduce the delayed cellular activation. Regarding *WSSinput*, after initializing each ABM site of the lumen wall with the corresponding CFD-derived WSS, a level of endothelial dysfunction $D \in (0; 1)$ was computed at the lumen wall sites, with higher values associated to low WSS and vice-versa (Chistiakov et al., 2017). D was defined as sigmoid shaped function of the WSS (Corti et al., 2022):

$$D(WSS)^i = \ -\frac{1}{1+e^{L_1(WSS^i-L_2)}} + 1 \qquad (4)$$

where WSS^i is the value of WSS at the ith lumen wall site and L_1=-15.25 [Pa^{-1}] and L_2=0.5 [Pa] define the slope and the WSS value at which $D = 0.5$, respectively (Supplementary Fig. S1). The values of L_1 and L_2 were set at the half admittable ranges, defined as the combination of L_1 and L_2 that guarantee D(WSS=0)>0.9 and D(WSS=1)<0.1 (Corti et al., 2022). While at the lumen wall sites *WSSinput* was constituted by the above described variable D (representing the endothelial

dysfunction), in the intima sites the effect of the WSS propagated as described by Eq. 5 (Corti et al., 2022):

$$WSSinput = \begin{cases} D^i & lumen\ wall\ sites \\ \sum_i D(WSS)^i \times Amp \times (1 + \cos\left(\pi\frac{x}{dist}\right)) & intima\ sites \end{cases} \quad (5)$$

According to Eq. 5, D was hypothesized to spatially decay in the intima as the cosine curve portion with negative slope and amplitude $Amp = 0.09$ (Corti et al., 2022). At the intima sites at a distance x lower than 15 ABM sites ($dist = 15$ ABM sites) from the lumen wall sites i, $WSSinput$ consisted in the sum of the decays of D.
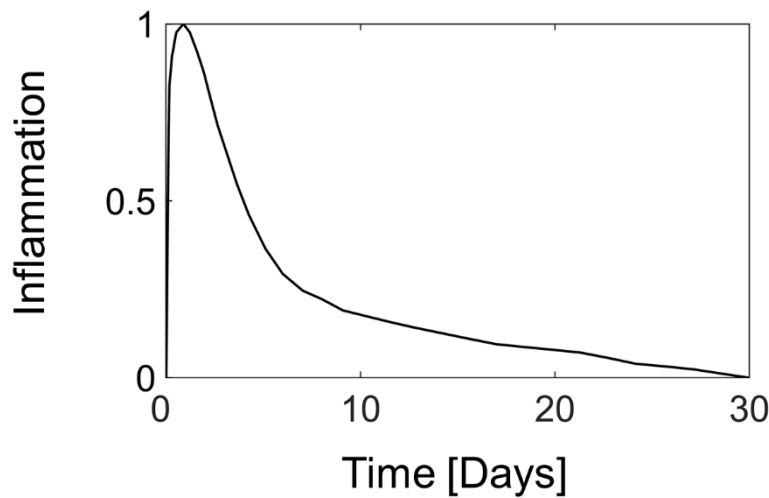

Figure 5. Generic inflammatory curve, inspired from literature (Edelman and Rogers, 1998).

To desynchronize agent dynamics (i.e., to randomize the cellular activities), each agent was associated with a random even number, representing its biological time (internal clock), between 0 and T_{agent} (T_{cell}=24 hours and T_{ECM}=4 hours, being T the agent biological cycle), which was updated at each ABM time step (2 hours). Accordingly, each potentially active agent, namely an agent at the end of its biological cycle (i.e., internal clock=T_{agent}), was randomly interrogated at each time step,

18

to assess whether it underwent a biological event or not. Specifically, a random number $test \in (0; 1)$ was generated. Then, if the agent event probability (mitosis/apoptosis for cell agents, or ECM production/degradation for cell and ECM agents) was greater than $test$, then the agent became an active agent undergoing the specific event. Once the active agent underwent the biological event, its biological clock was reset, together with that of the potential newly born agent. In the media and adventitia layers, which were assumed not to be involved in the restenosis process, baseline cell mitosis/apoptosis and ECM production/degradation probabilities were defined as in (Corti et al., 2020). In the intima, the biomechanical post-intervention inputs $Dinput$ and $WSSinput$ influenced the agent-specific cell mitosis and ECM production, while cell apoptosis and ECM degradation were maintained at their baseline values. Thus, the set of agent dynamics probabilities was defined as follows:

$$
intima: \begin{cases} p_{division}^h = \alpha_1 + \alpha_2 WSSinput^h + \alpha_3 Dinput^h \\ p_{apoptosis}^h = \alpha_1 \\ p_{ECMproduction}^h = \alpha_4 + \alpha_5 WSSinput^h + \alpha_6 Dinput^h \\ p_{ECMdegradation}^h = \alpha_4/\beta_{int} \end{cases} \tag{6}
$$

$$
media/adventitia: \begin{cases} p_{division}^h = p_{apoptosis}^h = \alpha_1 \\ p_{ECMproduction}^h = \beta_{med/adv} \cdot p_{ECMdegradation}^h = \alpha_4 \end{cases} \tag{7}
$$

where α_1=0.05 and α_4=0.008 were previously set (Corti et al., 2020) and α_2=0.06, α_3=0.65, α_5=0.019, α_6=0.25, β_{int}=1.55, β_{med}=1.55 and β_{adv}=2.5. The ABM parameter values introduced in Eqs. 4-7 were either derived from previous works (Corti et al., 2022, 2020, 2019) or tuned to obtain a degree of restenosis coherent with clinical studies in human femoral arteries (Wyttenbach et al., 2004), reporting a lumen area loss of about 25% at 3-month as compared to the condition immediately after PTA. Furthermore, the determined parameter values guaranteed a final intimal ECM/SMC ratio (normalized on the initial value) falling in the range [0.5 1.5], according to the hypothesis that no extreme changes over time occur in the intimal ECM/SMC ratio within the first post-operative months (Chung et al., 2002; Kearney et al., 1997; Strauss et al., 1992). To this aim,

19

to compensate the biased ECM production over cell proliferation, which is due to the higher baseline ECM content with respect to the cellular one, the values of the parameters related to the cellular dynamics were set to be higher than those related to the ECM dynamics. Finally, the β coefficients were introduced and calibrated to guarantee the maintenance of ECM content under baseline conditions (Corti et al., 2020).

As extensively described in (Corti et al., 2020), agent generation (in case of cell mitosis or ECM production) and agent removal (in case of cell apoptosis or ECM degradation) was inward-oriented in the intima, or outward-oriented in media and adventitia. Briefly, the inward oriented dynamics (referred to the intima layer only) implies that the production of new agents determines intimal growth with subsequent lumen narrowing, while agent degradation leads to arterial wall thinning by increasing the lumen area. Conversely, the outward oriented agent dynamics (referred to the media and adventitia layers) implies that the production of new elements determines tissue growth with external diameter enlargement, without lumen narrowing), while element degradation leads to arterial wall thinning by reducing the external diameter and preserving the lumen area. Finally, to maintain smooth and regular contours, the following regularization steps were performed: (i) contact maximization for border agents, (ii) preservation of the original internal elastic lamina, and (iii) circular approximation (with current average radius) of the external elastic lamina and the external border.

Due to the stochastic ABM nature, 3 repetitions were run for each simulation (i.e., each cross-section). Accordingly, at the end of the 3 repetitions, the output minimizing the root mean square deviation of the lumen contour from the average one was selected for each cross-section (Corti et al., 2022, 2020). The follow-up arterial lumen surface was then reconstructed by smoothly connecting the lumen contours of the ABM cross-sections.

2.2. ABM testing: 2D idealized scenarios

Before applying the developed multiscale framework of restenosis, the working mechanisms of the 2D ABM of arterial wall remodeling described in Section 2.1.4 were verified by performing 2D ABM simulations on a single cross-section (cross-section 1 of Fig. 3) of the 3D SFA geometry, considering idealized scenarios characterized by artificially-generated *Dinput* and *WSSinput*. Specifically, 11 scenarios (detailed in Table 6) were generated from the combination of the damage and WSS input stimuli shown in Fig. 6. In the scenarios 1-5, only one biomechanical input, either *Dinput* or *WSSinput*, was considered. In the scenarios 6-11, combined inputs were considered. Three conditions of *Dinput* were generated (Fig. 6), by defining: (i) a symmetric, uniformly distributed damage equal to 0.5 (chosen as representative of a mid-level of damage), (ii) a non-symmetric, localized damage at the bottom-left portion of the cross-section, reaching a peak of 1, and (iii) a non-symmetric, localized damage at the top-right portion of the cross-section, reaching a peak of 1. Similarly, 2 conditions of *WSSinput* were generated through the definition of: (i) a uniform WSS equal to 0.4 Pa (computed considering a Poiseuille flow), and (ii) a non-symmetric WSS with low WSS (WSS<0.4 Pa) localized at the top-right portion of the cross-section (Fig. 6). For each scenario, the 1-month follow-up was analyzed by running 3 repeated simulations.

Table 6. Idealized scenarios of damage- and wall shear stress-based inputs

Scenario	1	2	3	4	5	6	7	8	9	10	11
Damage	Abs	Abs	S	NS-L	NS-R	S	NS-L	NS-R	S	NS-L	NS-R
WSS	S	NS	Abs	Abs	Abs	S	S	S	NS	NS	NS

Abs: absent; S: symmetric; NS: non-symmetric; NS-L: non-symmetric left; NS-R: non-symmetric right

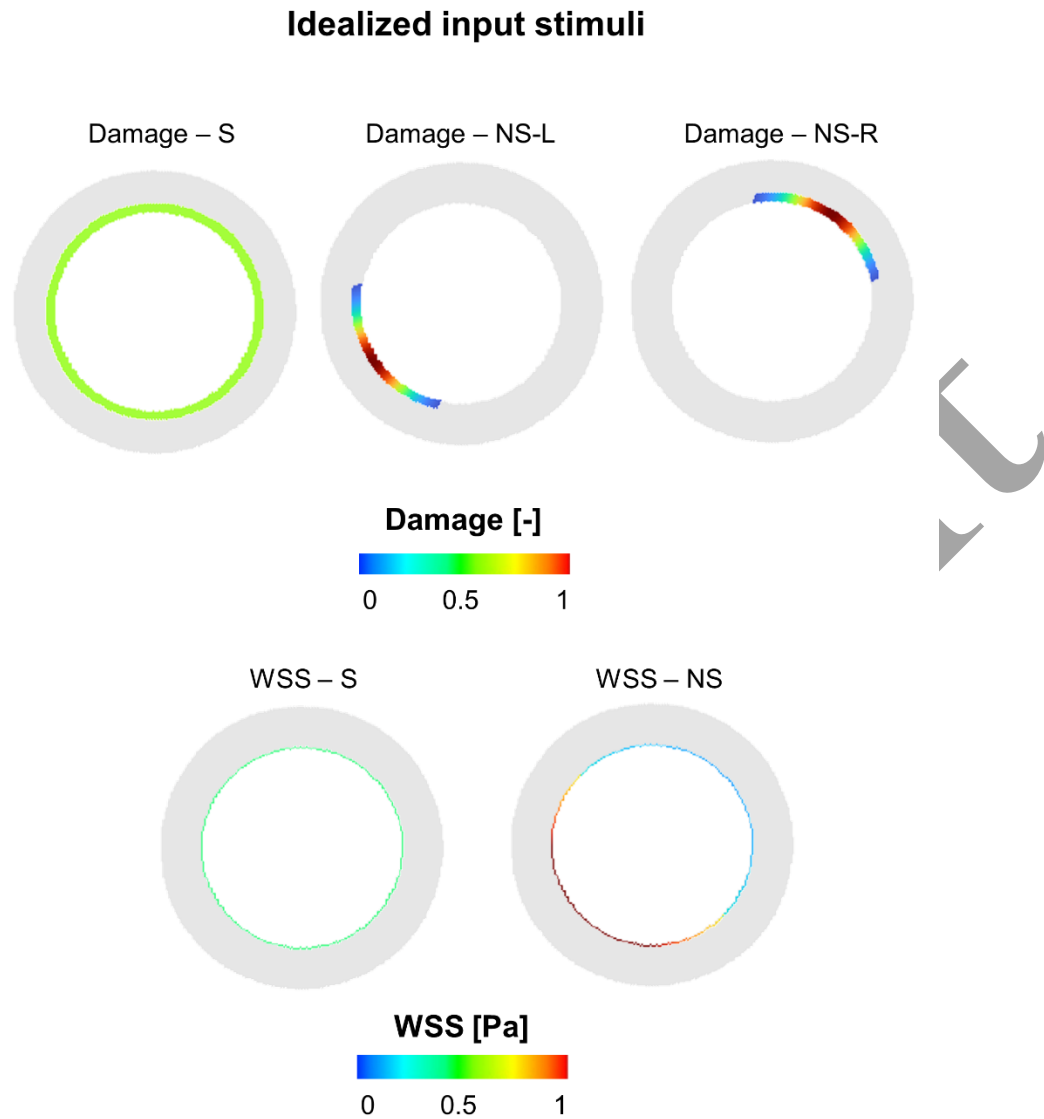**Idealized input stimuli**

Figure 6. Damage and wall shear stress (WSS) input stimuli imposed to generate the 11 idealized scenarios. At the top, the three damage conditions: symmetric (S), non-symmetric left (NS-L) and non-symmetric right (NS-R). At the bottom the two WSS conditions: symmetric (S) and non-symmetric (NS).

3. Results

3.1. 2D ABM simulations under idealized scenarios

Figures 7 and 8 show the 1-month evolution (day 0, 10, 20, 30) of the ABM plane 1 for the single-input scenarios (1-5 in Table 6) and the combined-input scenarios (6-11 in Table 6), respectively. Figure 9 illustrates the corresponding normalized lumen area over time. In line with the expectations: (i) a greater intima thickening was observed in correspondence of low WSS or

22

high damage values, (ii) uniform intima distribution was generated under symmetric-input scenarios, while focal, non-symmetric intima growth was obtained under non-symmetric-input scenarios, and (iii) output configurations resulting from combined-input scenarios presented a superimposition of the effects of the single inputs. The temporal trends of the lumen area related to the single-input scenarios (1-5 in Table 6) exhibited the following two distinct behaviors associated with the input types (Fig. 9A): (i) linear lumen area decrease due to the constant *WSSinput* (scenarios 1-2) and (ii) 4-phase lumen area dynamics due to the time-varying *Dinput* (scenarios 3-5), consisting in maintenance until day 3 (silent *Dinput*), abrupt decrease from day 3 (*Dinput* activation), decrease attenuation around day 8 (*Dinput* decay), and stabilization after about day 20 (decrease in slope of *Dinput*). The temporal trends of the lumen area related to the combined-input scenarios (6-11 in Table 6) presented a 4-phase lumen area dynamics (Fig. 9B). The presence of 4 phases was associated to the time-varying *Dinput*. However, *WSSinput* contributed to the temporal trends of lumen area, by determining, for example, a linear lumen area decrease in phases 1 and 4, instead of the constant behaviors observed in Fig. 9A (scenarios 3-5). In all cases, the normalized intimal ECM/SMC ratio lied within the admissible range (Supplementary Fig. S2). The ABM repeatability was confirmed by the small interquartile range (Fig. 9) and the high similarity of the 1-month outputs resulting from the 3 repetitions of each scenario (Supplementary Figs. S3-S4). The overall results verified the ABM, by providing a consistency check with the governing hypotheses and working mechanisms.
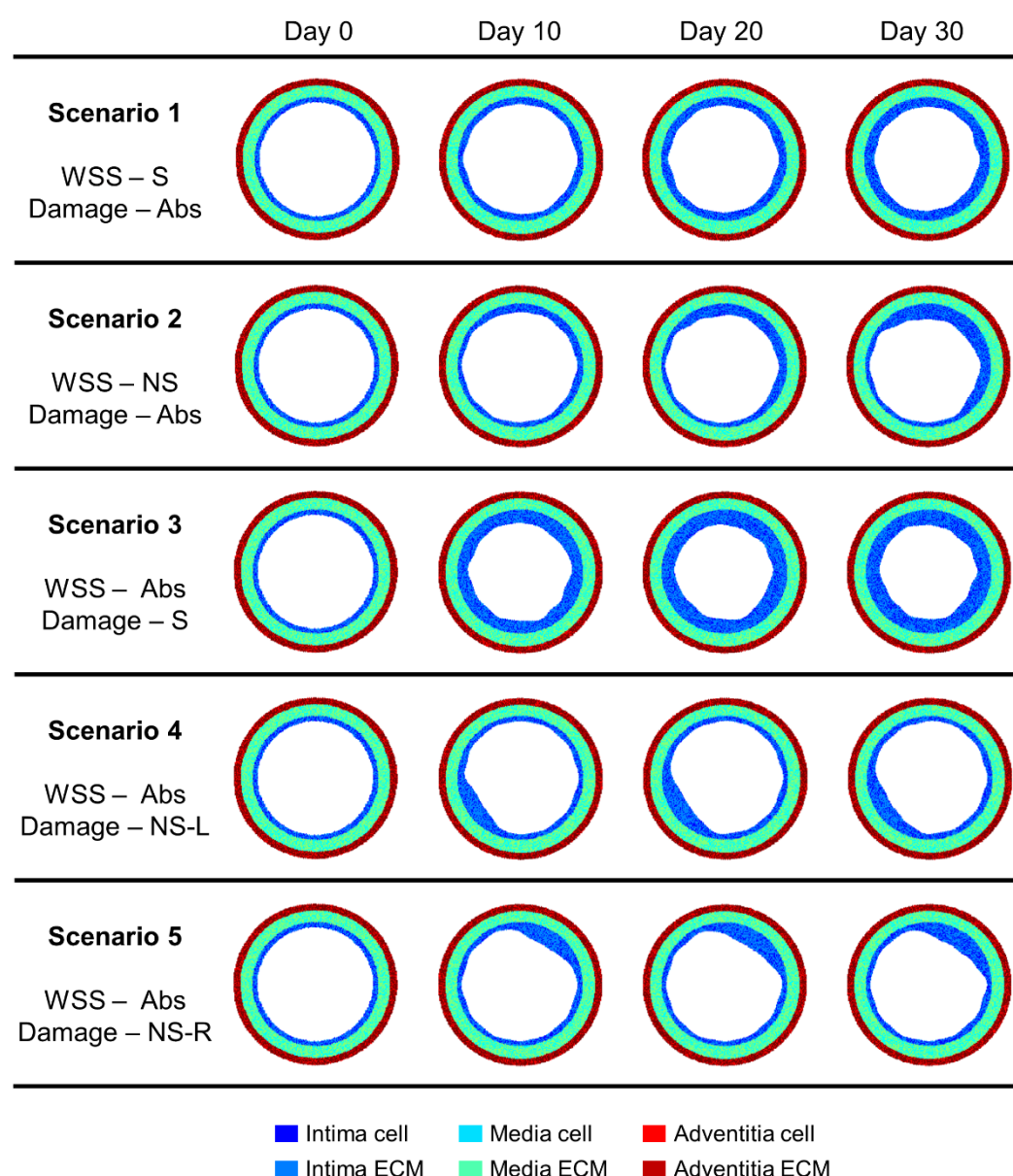
Figure 7. Temporal evolution of the agent-based model (ABM) simulations under the idealized scenarios 1-5, along 1 simulated month (day 0, day 10, day 20 and day 30). For each ABM plane, the results were retrieved from 1 out of 3 ABM simulations, namely the one presenting the lumen configuration minimizing the root mean square deviation, as detailed in Section 2.1.4.
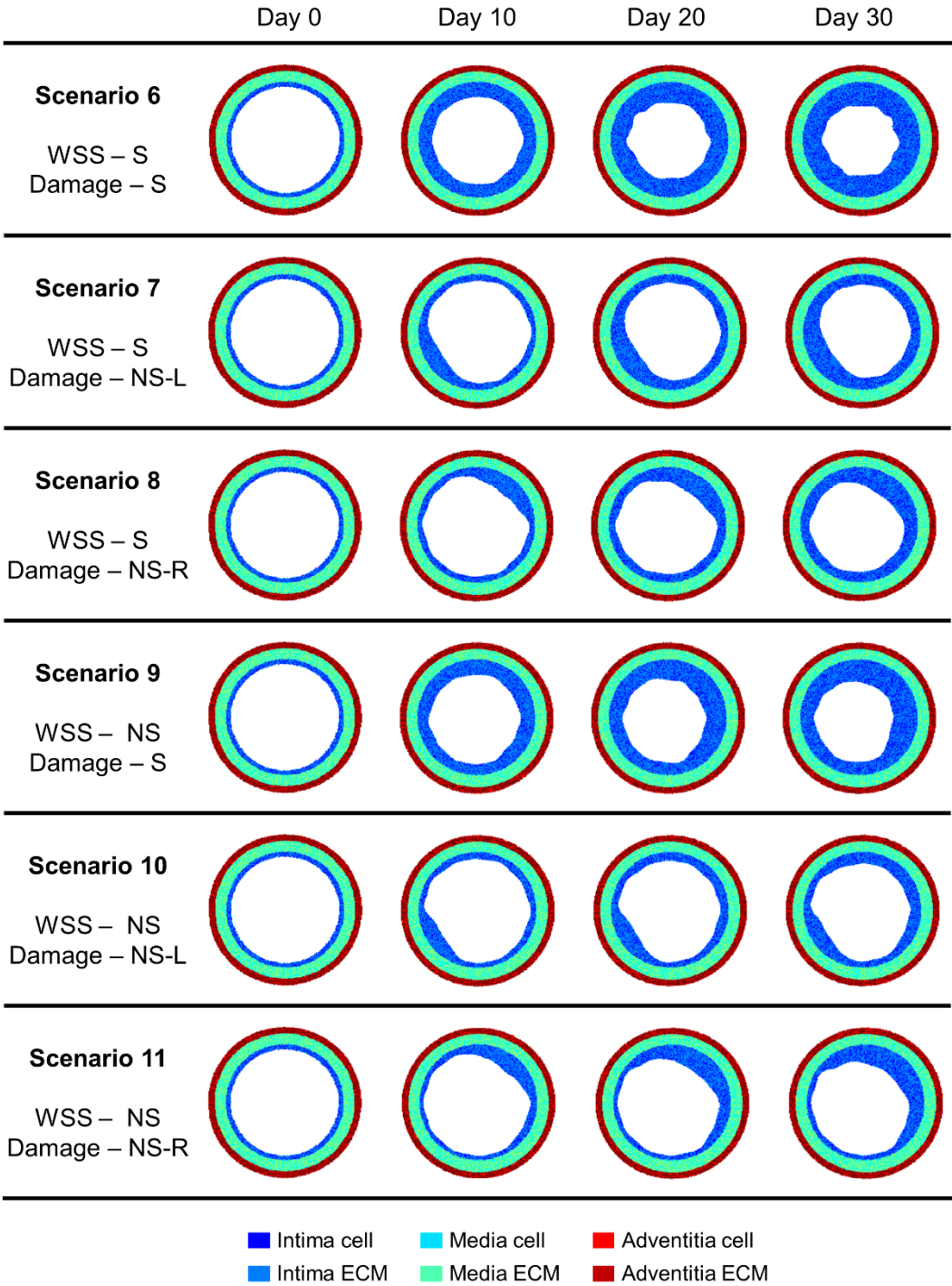
Figure 8. Temporal evolution of the agent-based model (ABM) simulations under the idealized scenarios 6-11, along 1 simulated month (day 0, day 10, day 20 and day 30). For each ABM plane, the results were retrieved from 1 out of 3 ABM simulations, namely the one presenting the lumen configuration minimizing the root mean square deviation, as detailed in Section 2.1.4
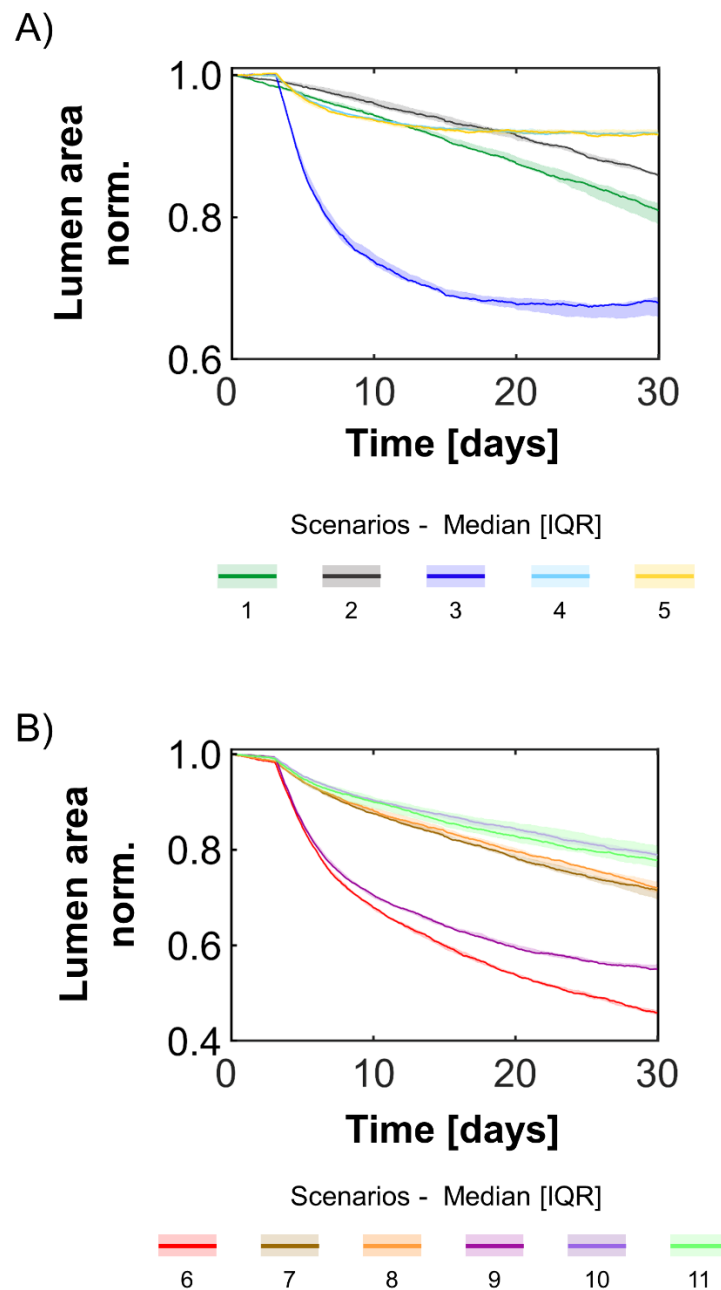
Figure 9. A) Normalized lumen area over time of the agent-based model (ABM) simulations under the idealized scenarios 1-5, along 1 simulated month. B) Normalized lumen area over time of the ABM simulations under the idealized scenarios 6-11, along 1 simulated month. The results of panels A and B represent the median and interquartile range (IQR) obtained from 3 ABM simulations of each scenario.

3.2. 3D idealized SFA model: 3-month restenosis simulation

The virtual PTA procedure performed in the diseased SFA model allowed obtaining a lumen area increase of ~25% in the treated portion, compared to the pressurized vessel configuration (Fig.

26

10A). After the procedure, a residual stenosis of ~35% was still present at the most stenotic plane (plane 10, Fig. 10A). The PTA procedure (Supplementary Video V1) induced a mild damage, mainly localized in the intima layer on the plaque side, with maximum values ~0.35 in the most stenotic plane (plane 10, Fig. 10B). The post-PTA vessel lumen geometry (Fig. 11A, day 0) was extracted and used to perform the CFD simulation. The WSS computed in the post-PTA vessel lumen configuration are shown in Fig. 11A (day 0). Except for the atherosclerotic region, the post-PTA vessel lumen geometry presented WSS lower than 1 Pa, with very low WSS (<0.1 Pa) downstream from the plaque.

Both the PTA-induced damage (Fig. 10B) and the WSS profile at time 0 (Fig. 11A, day 0) were used to drive the 1-month arterial wall remodeling computed by the ABM. As explained in Section 2.1.4, at the monthly coupling times (i.e., at 1- and 2-month follow-ups) the vessel lumen geometry was reconstructed from the ABM outputs, the WSS was re-computed in the current geometry and the ABM re-initialized with the updated hemodynamic input. Figure 11A (months 1, 2 and 3) depicts the reconstructed ABM-derived lumen surface at 1-, 2- and 3-month follow-ups with the corresponding WSS profile.
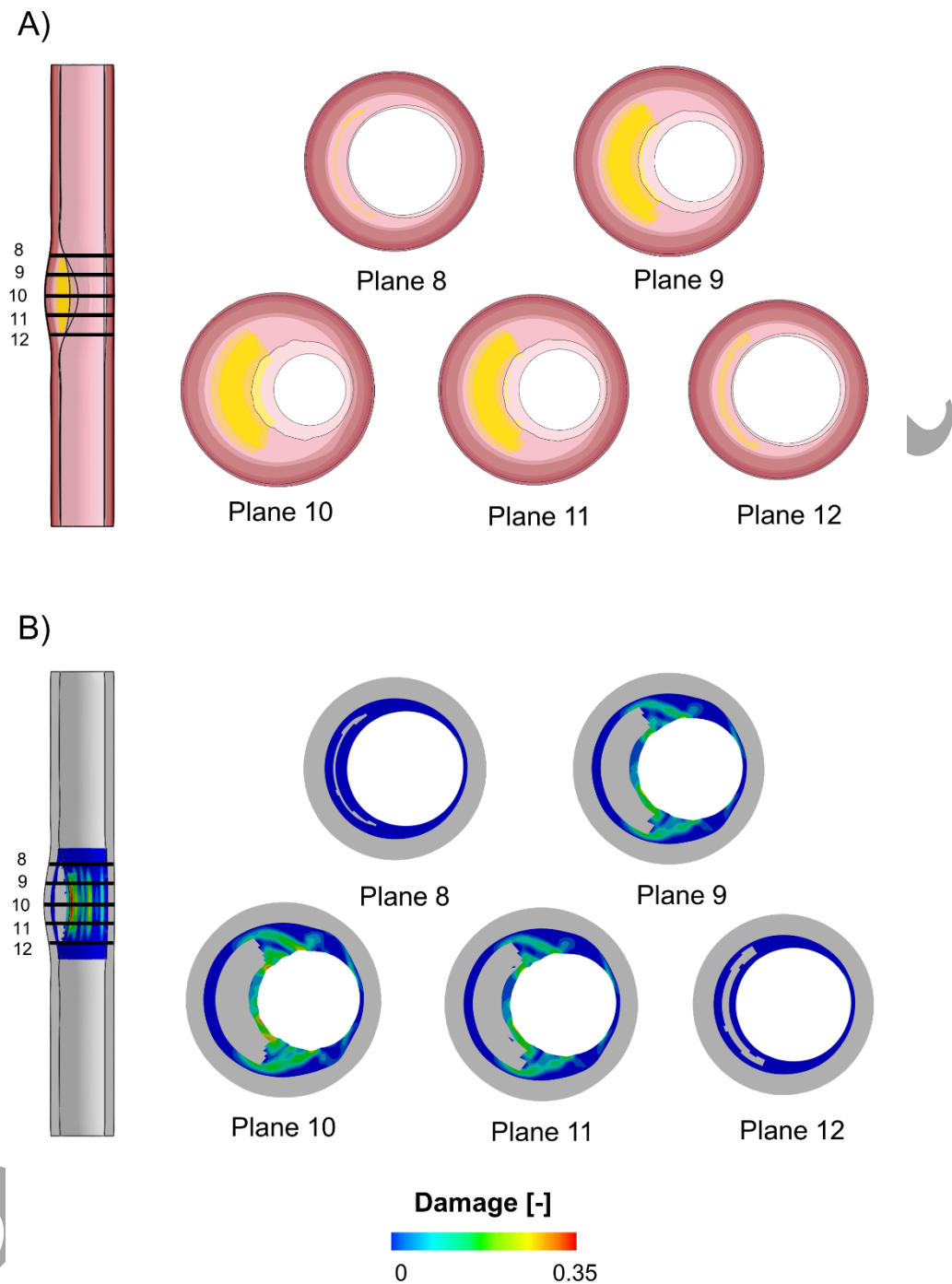
Figure 10. Results of the percutaneous transluminal angioplasty (PTA) simulation. A) Superimposed initial and deformed configurations. B) Damage map computed within the PTA module.
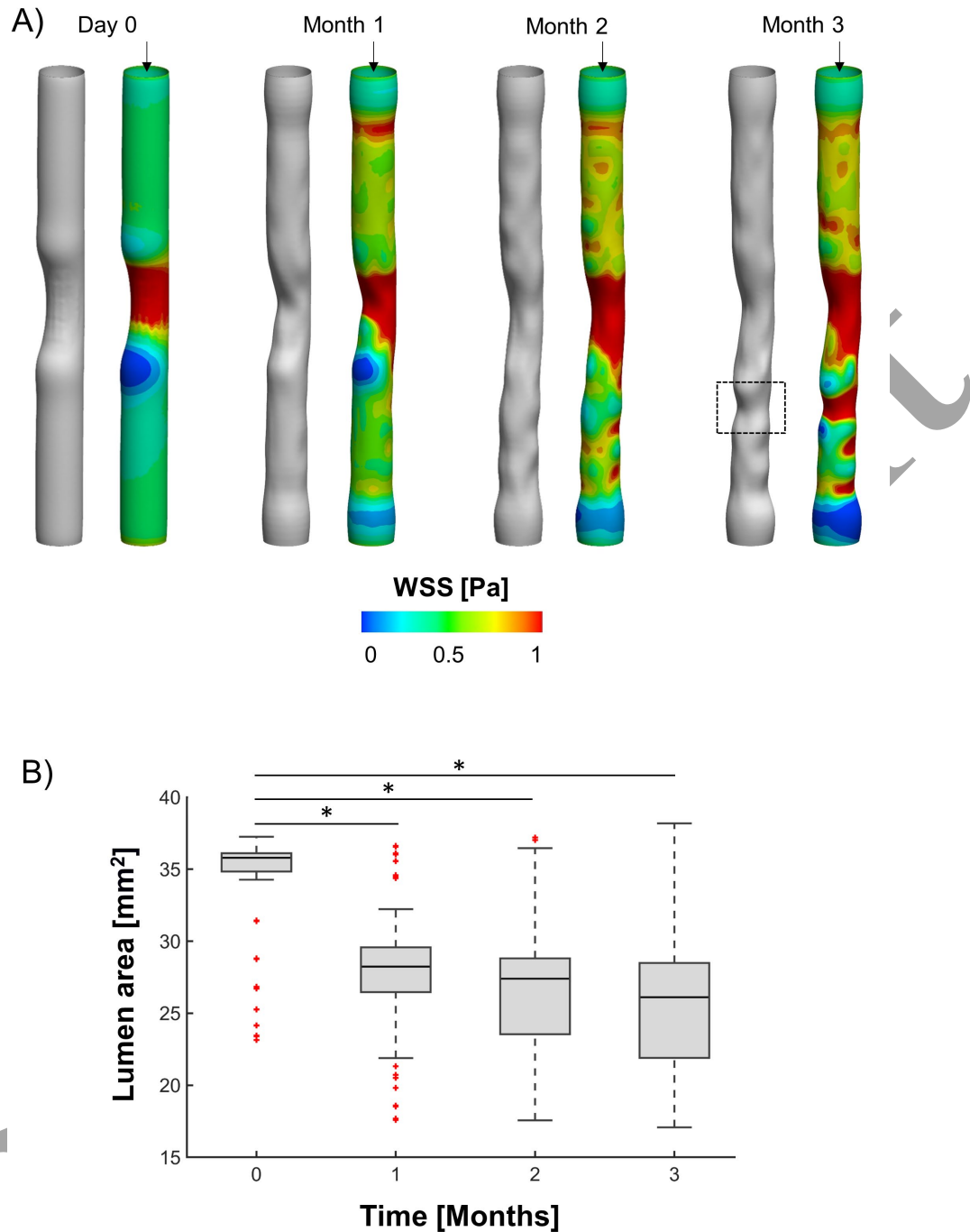
Figure 11. A) Lumen surface and wall shear stress (WSS) contour at day 0, month 1, month 2 and month 3. The lumen surface at day 0 was extracted from the deformed configuration computed by the percutaneous transluminal angioplasty (PTA) module. The lumen surface at month 1, month 2 and month 3 was reconstructed from the agent-based model outputs, as detailed in Section 2.1.4. B) Boxplots of the lumen area of the three-dimensional geometry immediately after the intervention (0), at month 1, month 2 and month 3. The lumen area was computed by considering 1 mm axially-spaced vessel cross-sections. Kruskal-Wallis test with multiple comparison was used to compare the 3 groups. * p-value < 0.05 (p-value correction through Tukey-Kramer method).

The temporal evolution of 7 explanatory ABM planes (i.e., plane 5 in the proximal region, planes 9, 10 and 11 in the atherosclerotic region and planes 13, 15 and 17 in the distal region) at day 0 and at 1-, 2- and 3-month follow-ups are shown in Fig. 12 and Supplementary Video V2. The displayed ABM monthly output of each plane corresponded to the one selected (among the 3 repeated simulations) at the monthly coupling time. For the sake of completeness, the outputs of 3 repeated simulations at the monthly coupling time are illustrated in Supplementary Fig. S5 (planes 5, 9, 10, 11, 13, 15 and 17). Figure 13 depicts, for the 7 explanatory planes, the temporal trends of the normalized lumen, intima, media and adventitia areas, intimal SMC and ECM content, and normalized intimal ECM/SMC ratio, resulting from the 3 repeated ABM simulations. The 7 planes experienced different degree and distribution of intimal growth and remodeling (and subsequent lumen narrowing), coherently with the different biomechanical stimuli (Figs. 12-13). Specifically, in the proximal region, plane 5, exposed to uniform WSS (~0.4 Pa) and null damage, underwent a ~20% uniform lumen area reduction. In the atherosclerotic region, plane 9, exposed to a WSS > 1 Pa and low damage level, underwent a ~10% lumen area reduction, and planes 10 and 11, exposed to a WSS > 1 Pa and mild damage level, underwent a ~25% lumen area reduction. In said planes a greater intimal growth was observed at the plaque side, corresponding to the mostly damaged location. In the distal region, planes 13, 15 and 17, exposed to low WSS and no damage, underwent a lumen area reduction of ~ 40%, 50% and 35%, respectively, with accentuated intimal growth at the low-WSS locations in planes 13 and 15 and uniform intimal distribution in plane 17. As evincible from the ABM outputs (Figs. 12-13) and from the lumen surfaces reconstructed at the 3 follow-up time points (Fig. 11A, months 1, 2 and 3), the region downstream the atherosclerotic lesion experienced a substantial arterial wall remodeling with critical focal lumen area reduction.

While planes 9, 10 and 11 exhibited the 4-phase temporal dynamics (Fig. 13) associated with the *Dinput*, planes 5, 13, 15 and 17 presented the linear dynamics associated with the *WSSinput*, with slope changes at the coupling times (months 1, 2), due to the hemodynamics update

in the monthly reconstructed geometry (Fig. 11A). To this regard, the mutual interaction between arterial wall remodeling and hemodynamics was well captured by the model. As emerged from Fig. 11A and from the lumen area trend of Fig. 13, the initial (i.e., immediately after PTA) low-WSS region downstream the atherosclerotic region (around plane 13) underwent a hemodynamic-driven lumen area reduction in the first 2-months follow-up, leading to a progressive increase of the WSS, which slowed down the restenosis process. Consequently, at month 2, the low WSS region translated distally (toward plane 15), speeding up the restenosis process and provoking the 3-month focal ~50% restenosis (dashed box, Figure 11A, month 3). Overall, these results highlighted the importance of the hemodynamics update in the simulation of the remodeling process, allowing capturing the mutual interaction between hemodynamics and arterial lumen remodeling.

As expected, the intima was the only layer involved in the restenosis process, undergoing up to 3-fold area growth (planes 13, 15 and 17), while the media and adventitia preserved their initial areas (Fig. 13). Moreover, although planes 9, 10 and 11 underwent a non-negligible lumen area decrease (similar to that of plane 5) due to intimal growth, the normalized intima area evolution of said planes was substantially different from that of the other planes (Fig. 13). This was mainly attributable to the greater initial intimal area of planes 9, 10 and 11 (in the atherosclerotic region) compared to all the others. For all the planes, both the ECM and SMC agents contributed to the intimal growth and the normalized intimal EMC/SMC ratio over time remained within the desired range [0.5 1.5] throughout the entire simulation time. Finally, the repeatability of the model was evincible from the small interquartile range (Fig. 13) and the high similarity of the outputs resulting from the 3 repetitions of each plane (Supplementary Fig. S5). Similar considerations held for all the considered 19 planes.

The multiscale framework simulated a median 27% restenosis at 3-month follow-up, with a progressive lumen area reduction, from an initial median lumen area of 35.8 [34.8 – 36.1] mm^2 to a final median lumen area of 26.1 [21.9 – 28.5] mm^2 (Fig. 11B). The median lumen area was computed as by considering 1 mm axially-spaced vessel cross-sections. Moreover, the greatest

lumen area reduction was observed at 1-month follow-up with respect to the post-PTA condition ($p<0.05$), while not-significant lumen area reduction was found in the following months. Finally, the simulated lumen area presented an increased dispersion over time. Overall, the multiscale model successfully captured relevant features of the post-operative arterial wall remodeling, providing a good replication of the lumen area trend along the first 3 post-operative months.
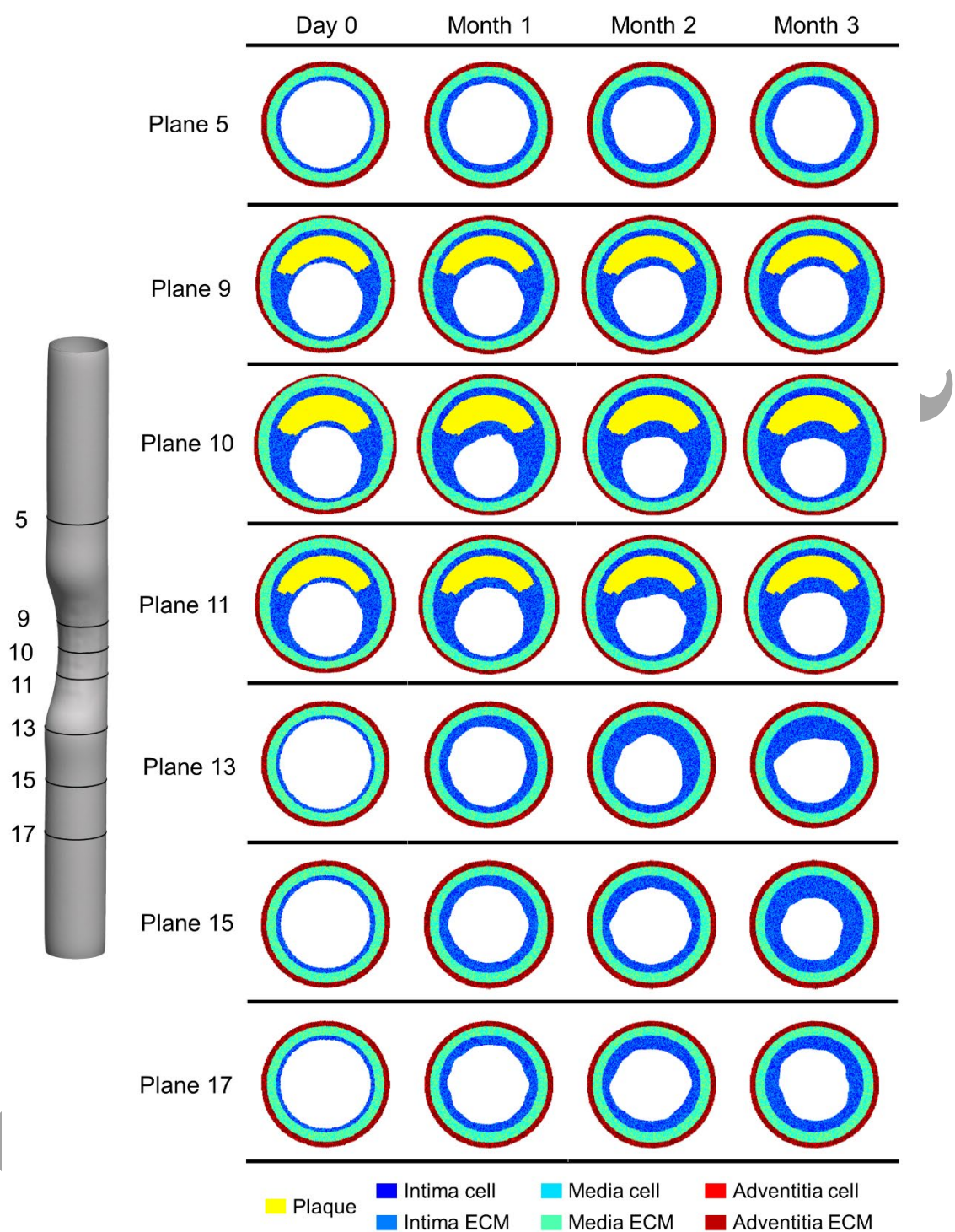
Figure 12. Temporal evolution of the agent-based models (ABM) of 7 explanatory planes (planes 5, 9, 10, 11, 13, 15 and 17) along 3 simulated months. For each ABM plane, the monthly output was retrieved from 1 out of 3 ABM simulations, namely the one presenting the lumen configuration minimizing the root mean square deviation, as detailed in Section 2.1.4.
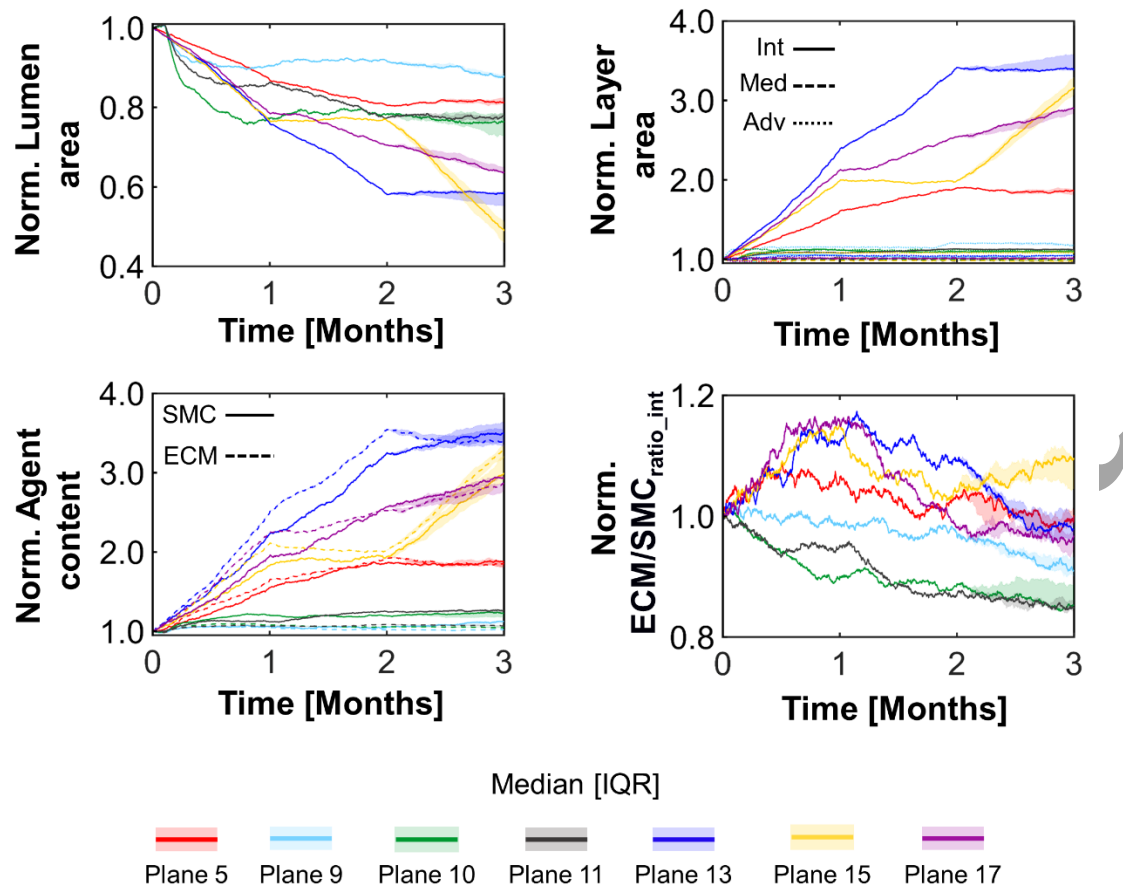
Figure 13. The temporal trends for planes 5, 9, 10, 11, 13, 15 and 17 of the normalized lumen area, the normalized area of the intima (solid line), media (dashed line) and adventitia (dotted line) layers, the normalized intimal content of smooth muscle cells (SMC) (solid line) and extracellular matrix (ECM) (dashed line) and the normalized intimal ECM/SMC ratio (ECM/SMC$_{ratio\_int}$) are shown along 3 simulated months. The median and interquartile range (IQR) obtained from 3 ABM simulations for each plane are shown.

4. Discussion

In this study, a novel multiscale agent-based modeling framework of restenosis at cell-tissue scale, replicating mechanobiological processes after PTA procedure, namely the early inflammatory-driven cellular activation due to the PTA-induced wall damage (*Dinput*) (Stefano et al., 2013) and the long-lasting hemodynamic-driven (*WSSinput*) arterial wall remodeling (Koskinas et al., 2012), was proposed. The framework was able to capture clinically relevant features of the lumen area median trend and dispersion over time following PTA, thus suggesting the potential

34

validity of the underlying hypotheses and of the model formulation. To this regard, this study further confirms that multiscale agent-based modeling frameworks, coupling continuum- with agent-based models within a systems biology approach, constitute a valid choice for capturing the complex, multiscale and multifactorial network of the underlying mechanobiological events involved in the arterial adaptation processes (Corti et al., 2021).

To date, several multiscale agent-based modeling framework of arterial wall remodeling following endovascular procedures (mainly focused on in-stent restenosis process) have been developed to investigate the effects of intervention-induced damage and/or hemodynamic disturbance on the subsequent cellular activities (Corti et al., 2021). Hoekstra's research group implemented a multiscale framework of in-stent restenosis in which the stent deployment procedure was simulated through an ABM that, through cell adhesion/repulsion rules, computed the structural equilibrium and the resulting post-stenting configuration and state of stress (Caiazzo et al., 2011; Tahir et al., 2014, 2013, 2011; Zun et al., 2019, 2017). To account for the intervention-induced damage, complete endothelial denudation was assumed, and a criterion was adopted according to which overstressed agents were removed. Following the stent-deployment module, the framework integrated a hemodynamics module (based on Lattice-Boltzmann method) and a tissue remodeling module (ABM) to capture the hemodynamic-driven arterial wall remodeling. Another stream of work (Boyle et al., 2011, 2010; Li et al., 2019; Nolan and Lally, 2018; Zahedmanesh et al., 2014) focused exclusively on the damage-induced in-stent restenosis and implemented a multiscale finite element (structural mechanics) – ABM framework in which the damage was computed as function of the von Mises stress resulting from the structural mechanics simulation of stent deployment (solved through the finite element method). Specifically, two damage model formulations were proposed, namely an instantaneous model (the damage was triggered at the injury time) and a cyclic damage model (the damage cumulated along the loading cycles). The resulting damage variable activated an inflammatory response, modeled through a set of ordinary differential equations describing the temporal evolution of growth and matrix degrading factors, which in turn constituted

35

the inputs for the ABM-simulated cellular activities. As compared to the studies of Hoekstra's research group (Caiazzo et al., 2011; Tahir et al., 2014, 2013, 2011; Zun et al., 2019, 2017), in these latter works (Boyle et al., 2011, 2010; Li et al., 2019; Nolan and Lally, 2018; Zahedmanesh et al., 2014) the effects of the hemodynamic disturbance on cellular activity were neglected, but a more reliable simulation of the stent-deployment procedure was performed (structural mechanics simulation vs. agent-based modeling approach) and more sophisticated damage and inflammatory models were proposed.

Overall, the previously described multiscale frameworks of arterial wall remodeling after stenting (Boyle et al., 2011, 2010; Caiazzo et al., 2011; Li et al., 2019; Nolan and Lally, 2018; Tahir et al., 2014, 2013, 2011; Zahedmanesh et al., 2014; Zun et al., 2017, 2019) were mainly focused on either the effects of damage or the hemodynamics on in-stent restenosis. Instead, to the authors' knowledge, the present study proposes the first multiscale agent-based modeling framework integrating: (i) a structural mechanics simulation of PTA in a diseased artery model, providing the post-intervention artery geometry and quantifying the arterial wall damage, and (ii) CFD simulations for computing the post-intervention hemodynamics with (iii) an ABM of arterial wall remodeling. Within the framework, each modeling tool was adopted for the purpose it was most suitable for, thus ensuring the optimization of the computational strategy. Although different, the damage formulation here implemented shared similar hypotheses with the instantaneous damage model proposed in (Nolan and Lally, 2018; Zahedmanesh et al., 2014). Indeed, the damage induced during the PTA was assumed as the major trigger of the early inflammatory response driving the cellular activation and the short-term arterial wall remodeling (i.e., within 1 post-operative month) (Stefano et al., 2013). Moreover, the cyclic coupling between the hemodynamics and the tissue remodeling modules allowed incorporating the long-term hemodynamic-driven arterial wall remodeling, similarly to the works of Hoekstra's research group (Caiazzo et al., 2011; Tahir et al., 2014, 2013, 2011; Zun et al., 2019, 2017). Compared to the previously proposed studies (Boyle et al., 2011, 2010; Caiazzo et al., 2011; Li et al., 2019; Nolan and Lally, 2018; Tahir et al., 2014,

2013, 2011; Zahedmanesh et al., 2014; Zun et al., 2017, 2019), this was the first time in which the multiscale model of restenosis was applied to a diseased artery model. The application of the framework to a diseased instead of healthy model (although idealized) constitutes a more realistic condition and offers the possibility to investigate the arterial wall response under different scenarios, for instance by modifying the plaque material (e.g., lipid, fibrous, or calcium).

The developed framework simulated the restenosis process following PTA procedure, capturing features that reflected clinical evidence. The simulated 27% lumen area reduction at 3-month follow-up (Figs. 11-13) was in accordance with the 3-month 25% lumen area loss in femoropopliteal arteries treated with PTA (Wyttenbach et al., 2004). The first post-operative month was characterized by the greatest lumen area reduction, while the overall growth process slowed down in the following months (Figs. 11-13), with the exception of a focal ~50% restenosis observed at 3-months follow-up (Fig. 11A, dashed box, and Fig. 13, plane 15). As shown in Fig. 11A (dashed box), the location of the focal restenosis was in accordance with evidence of disease progression downstream from the initial stenosis, due to the hemodynamic disturbance at this location (Koskinas et al., 2012). Moreover, the simulated temporal evolution of the lumen area reduction, as well as the increased lumen area dispersion over time reflected previous clinical findings (Colombo et al., 2021; Edelman and Rogers, 1998). Indeed, a 3-phase lumen area trend was observed in stented SFAs in the first post-operative year, characterized by (i) high lumen area reduction within 1-month follow-up, (ii) a stabilization phase until 6-months follow-up, and (iii) a potential focal lumen area reduction after 6 months (Colombo et al., 2021). Although the restenosis process simulated herein presented some discrepancies (mainly associated with the temporal windows, since here only 3-months follow-up were simulated) compared to the above-mentioned findings, the framework successfully captured the 3 phases characterizing the post-operative lumen area evolution, and the presence of focal narrowing.

Given the promising preliminary results in the idealized model of diseased SFA, future efforts must be focused on the model application to patient-specific vessel geometries and on its

verification, uncertainty quantification, calibration and validation. In this context, two main criticalities can be identified, namely: (i) the availability of proper patient-specific data for both the calibration and validation process, and (ii) the computational resources needed to perform an adequate number of simulations for the verification, uncertainty quantification, calibration and validation processes. As regards the computational demand, the original Matlab ABM code was converted to a C code through the Matlab coder toolbox, providing a substantial gain in time (up to 30 times faster). However, the current framework (with converted ABM code) still takes ~3 days to simulate 1 month (ABM and CFD simulations) using in parallel 19 cores (1 for each ABM plane) of a computer cluster equipped with quad-core Intel Xeon CPUs E5620 at 2.40 GHz, 24 GB RAM for each node, and INFINIBAND Mellanox for the main cluster interconnections. Subsequently, to afford the hundreds of simulations needed for the uncertainty and sensitivity analyses as well as for calibration, the use of surrogate models may become the only feasible solution, as done for example in (Corti et al., 2022; Nikishova et al., 2019; Ye et al., 2021).

Once properly validated, the framework could be used to gain further insights into the pathophysiological mechanisms of restenosis following PTA, by identifying critical factors enhancing the restenosis process, like the plaque composition, the balloon expansion pressure, the potential residual stenosis and the post-intervention hemodynamics, just to mention a few. Thus, application of the methodology to patient-specific cases will constitute a step forward towards the emerging personalized medicine, by contributing, through the identification of patient-specific disease mechanisms, to the development of tailored therapies. In this scenario, the omics sciences are recently receiving great attention, since they potentially allow for the detection of patient-specific biomarkers of the disease (e.g., genes, proteins), thus improving the disease prediction, diagnosis and treatment (Ouzounian et al., 2007). Said biomarkers, besides characterizing the patient pathological phenotype, constitute a promising therapeutic target through the development of genotype-based drugs (pharmacogenomics and pharmacoproteomics). Subsequently, the incorporation of multi-omics data in multiscale agent-based modeling frameworks of restenosis

would allow for a deeper understanding of the patient pathological pathways, providing a more comprehensive picture of the patient's disease through a multiscale, multifactorial and systems biology approach. Thanks to its modularity, the proposed framework could be enriched with gene-protein networks. By linking them to the cellular behaviors (e.g., by defining the dependency of specific cellular activities on the gene-protein expression level in the agent rules), it would be possible to identify gene-protein pathways whose up- or down-regulation may have an impact on the intervention outcome.

The present work is not exempt from limitations. As regards the PTA module, isotropic hyperelastic materials were used to model the arterial tissues, and a simple damage model was considered. However, the framework enables the use of more sophisticated damage models, describing the softening behavior of anisotropic hyperelastic materials under deformation (Rodríguez et al., 2006). Within the hemodynamics module, steady-state CFD simulations under the assumption of rigid walls were performed. Potentially, unsteady simulations can be performed in order to quantify the oscillatory nature of the WSS vector and its multi-directionality (Colombo et al., 2021; Hoogendoorn et al., 2020). To the authors' opinion, the rigid walls assumption is reasonable, considering the steady-state nature of the simulation and that the inclusion of wall motion was found to not significantly impact the global hemodynamics characteristics both in femoral (Kim et al., 2008) and in coronary arteries (Eslami et al., 2020). Regarding the tissue remodeling module, the ABM of arterial wall remodeling represents a simplification of the biological events involved in the arterial response to the intervention. Only cell mitosis and apoptosis and ECM production and degradation were simulated, and their changes according to the hemodynamics and damage-related inflammation were considered. In particular, our model simulated neointimal hyperplasia and subsequent restenosis as the result of the intervention-induced exacerbated synthetic and proliferative activities of SMCs in the intima triggered by hemodynamic and inflammatory cues. The inclusion of the underlying signaling pathways (e.g., release of growth factors and cytokines) involved in the SMC quiescent-to-synthetic phenotypic switch was beyond

the aim of the present study. Consequently, a phenomenological representation of the hemodynamic- and damage-induced SMC activation was proposed, which, although simplified, allowed to describe some of the main events involved in the process of restenosis. Indeed, synthetic SMCs, undergoing increased proliferation and ECM production in the intima, were identified as the key player of neointimal hyperplasia and restenosis (Chaabane et al., 2013; Marx et al., 2011). Moreover, since in this study SMC proliferation and ECM deposition in the intima were the only modeled cellular dynamics involved in the restenosis process, the damage induced during PTA, which modulates the resulting inflammatory response, was computed only in the intima layer of the diseased portion. SMC media to intima migration was neglected, although it is known to play a relevant role (Marx et al., 2011). The process of SMC migration from media to intima could be included in the future. However, in view of applying the framework to patient-specific arteries, the commonly available patient-specific data (e.g., lumen area, arterial wall thickness) would prevent from distinguishing between the contributions of migrating and synthetic SMCs in intimal growth, thus making the calibration of the two processes extremely challenging. Accordingly, although constituting a simplification, the increase of SMC within the intima, here simulated through the perturbation of intimal SMC mitosis, may account also for migrated SMCs, which start proliferating in the intima, and SMCs from other sources (e.g., pre-existing intimal SMCs or SMC progenitors (Chaabane et al., 2013)). In addition, consistent with the hypothesis that the events driving the arterial response to the intervention occur in the intima, SMCs in the media and fibroblasts in the adventitia were assumed not to be influenced by the intervention-induced damage (which was computed only in the intima layer). The behavior of these cells was described through baseline probabilities (i.e., leading to compensation of cell mitosis and apoptosis, and ECM production and degradation) resulting in a physiologic arterial wall remodeling. Hence, no distinction was assumed in the cellular dynamics of medial SMCs or adventitial fibroblasts. In addition, endothelial cells were not explicitly modeled, but a method was implemented to account for the direct and endothelial-mediated effects of WSS on SMC dynamics, as also proposed in the works of

40

Hoekstra's research group though with a different strategy (Tahir et al., 2014, 2013; Zun et al., 2019, 2017). Last, besides the aforementioned cellular events, additional cell-cell interactions and the effect of SMC paracrine signaling, which was found to have a relevant role in the arterial response to the intervention (Chaabane et al., 2013; Marx et al., 2011; Ren et al., 2019), could be included in the current ABM. Besides the specific limitations of each module, it must be considered that the framework was applied only on an idealized SFA anatomy, thus representing a proof-of-concept study. As previously discussed, future efforts must be focused on patient-specific applications and on calibrating and validating the framework. Finally, while the hemodynamics and tissue remodeling modules were bi-directionally coupled, the PTA module was run only once to simulate the PTA procedure and compute the post-intervention arterial geometry and the intervention-induced damage, thus providing the initial condition to the cyclic hemodynamics – tissue remodeling sequence. According to the hypotheses of the present work, the inflammatory response activated by the intervention-induced trauma, and the altered hemodynamics governed the arterial post-intervention remodeling. Thus, the damage induced by balloon expansion, corresponding to the maximum state of stress reached during the PTA simulation, was considered to modulate the inflammatory response, in turn affecting the ABM cellular activities. Subsequently, the ABM dynamics were influenced by the damage-induced inflammation rather than the internal state of stress. Further improvements of the framework might be the full coupling of all the modules, such that after a predefined coupling time the tissue remodeling module is coupled back, not only with the hemodynamics module, but also with a mechanical module, computing the state of stress in the deformed, remodeled geometry, as done in (Li et al., 2019). In this scenario, the ABM rules should be modified to account for the effect of the internal stress in arterial wall remodeling. While a full coupled framework would allow accounting for the mechanical equilibrium across all the modules, to the authors' opinion it would not markedly affect the final output. Indeed, a lowering of the internal stresses would be obtained in the remodeled geometry

(e.g., after 1 month), thus attenuating the arterial response, as already accounted for by considering the inflammatory curve (Fig. 5).

5. Conclusions

The developed multiscale agent-based modeling framework of restenosis replicated the 3-months arterial wall remodeling following PTA procedure in an idealized, diseased SFA model, by integrating the effects of the PTA-induced arterial wall damage and the post-intervention hemodynamics on cellular activity. The framework was able to capture relevant features of the arterial response to PTA intervention, including: (i) the increased intimal growth in the regions subjected to higher degree of injury and altered hemodynamics, (ii) a 3-month lumen area restenosis of ~25%, coherently with clinical observations for the SFA at that follow-up (Wyttenbach et al., 2004), and (iii) a 3-phase lumen area trend over time (in line with the typical phases of restenosis in SFA (Colombo et al., 2021)), resulting from the mutual interaction of the mechanobiological processes triggered by the two different inputs (i.e., *Dinput* and *WSSinput*). In addition, the feasibility of linking different software in an automated computational framework and the potentiality of the multifactorial, multiscale and systems biology approach in simulating the underlying mechanisms of complex vascular adaptation processes were highlighted. Considering the results provided herein, the developed framework lays the foundation towards an in-silico model of restenosis, promising to capture the overall lumen area remodeling following endovascular interventions in patient-specific scenarios.

Declarations

Funding

42

Conflicts of interest

The authors declare that they have no conflict of interest.

References

Antonini, L., Berti, F., Isella, B., Hossain, D., Mandelli, L., Pennati, G., Petrini, L., 2021. From the real device to the digital twin: A coupled experimental-numerical strategy to investigate a novel bioresorbable vascular scaffold. *PloS one* 16, e0252788. https://doi.org/10.1371/journal.pone.0252788

Boyle, C.J., Lennon, A.B., Early, M., Kelly, D.J., Lally, C., Prendergast, P.J., 2010. Computational simulation methodologies for mechanobiological modelling: a cell-centred approach to neointima development in stents. *Philosophical Transactions of the Royal Society A: Mathematical, Physical and Engineering Sciences* 368, 2919–2935. https://doi.org/10.1098/rsta.2010.0071

Boyle, C.J., Lennon, A.B., Prendergast, P.J., 2011. In silico prediction of the mechanobiological response of arterial tissue: application to angioplasty and stenting. *Journal of Biomechanical Engineering* 133, 081001. https://doi.org/10.1115/1.4004492

Caiazzo, A., Evans, D., Falcone, J.L., Hegewald, J., Lorenz, E., Stahl, B., Wang, D., Bernsdorf, J., Chopard, B., Gunn, J., Hose, R., Krafczyk, M., Lawford, P., Smallwood, R., Walker, D., Hoekstra, A., 2011. A Complex automata approach for in-stent restenosis: two-dimensional

multiscale modelling and simulations. *Journal of Computational Science* 2, 9–17. https://doi.org/10.1016/j.jocs.2010.09.002

Chaabane, C., Otsuka, F., Virmani, R., Bochaton-Piallat, M.L., 2013. Biological responses in stented arteries. *Cardiovascular Research* 99, 353–363. https://doi.org/10.1093/cvr/cvt115

Chiastra, C., Grundeken, M.J., Collet, C., Wu, W., Wykrzykowska, J.J., Pennati, G., Dubini, G., Migliavacca, F., 2018. Biomechanical Impact of Wrong Positioning of a Dedicated Stent for Coronary Bifurcations: A Virtual Bench Testing Study. *Cardiovascular engineering and technology* 9, 415–426. https://doi.org/10.1007/s13239-018-0359-9

Chiastra, C., Iannaccone, F., Grundeken, M.J., Gijsen, F.J.H., Segers, P., De Beule, M., Serruys, P.W., Wykrzykowska, J.J., van der Steen, A.F.W., Wentzel, J.J., 2016a. Coronary fractional flow reserve measurements of a stenosed side branch: a computational study investigating the influence of the bifurcation angle. *BioMedical Engineering OnLine* 15, 91. https://doi.org/10.1186/s12938-016-0211-0

Chiastra, C., Wu, W., Dickerhoff, B., Aleiou, A., Dubini, G., Otake, H., Migliavacca, F., LaDisa, J.F.J., 2016b. Computational replication of the patient-specific stenting procedure for coronary artery bifurcations: From OCT and CT imaging to structural and hemodynamics analyses. *Journal of biomechanics* 49, 2102–2111. https://doi.org/10.1016/j.jbiomech.2015.11.024

Chistiakov, D.A., Orekhov, A.N., Bobryshev, Y. V, 2017. Effects of shear stress on endothelial cells: go with the flow. *Acta physiologica (Oxford, England)* 219, 382–408. https://doi.org/10.1111/apha.12725

Chung, I.M., Gold, H.K., Schwartz, S.M., Ikari, Y., Reidy, M.A., Wight, T.N., 2002. Enhanced extracellular matrix accumulation in restenosis of coronary arteries after stent deployment. *Journal of the American College of Cardiology* 40, 2072–2081. https://doi.org/10.1016/S0735-1097(02)02598-6

Colombo, M., He, Y., Corti, A., Gallo, D., Ninno, F., Casarin, S., Rozowsky, J.M., Migliavacca, F., Berceli, S., Chiastra, C., 2021. In-Stent Restenosis Progression in Human Superficial Femoral

Arteries: Dynamics of Lumen Remodeling and Impact of Local Hemodynamics. *Annals of Biomedical Engineering* 49, 2349–2364. https://doi.org/10.1007/s10439-021-02776-1

Corti, A., Casarin, S., Chiastra, C., Colombo, M., Migliavacca, F., Garbey, M., 2019. A Multiscale Model of Atherosclerotic Plaque Development: Toward a Coupling Between an Agent-Based Model and CFD Simulations, in: Rodrigues, J.M.F., Cardoso, P.J.S., Monteiro, J., Lam, R., Krzhizhanovskaya, V. V, Lees, M.H., Dongarra, J.J., Sloot, P.M.A. (Eds.), Computational Science -- ICCS 2019. Springer International Publishing, Cham, pp. 410–423.

Corti, A., Chiastra, C., Colombo, M., Garbey, M., Migliavacca, F., Casarin, S., 2020. A fully coupled computational fluid dynamics – agent-based model of atherosclerotic plaque development: Multiscale modeling framework and parameter sensitivity analysis. *Computers in Biology and Medicine* 118, 103623. https://doi.org/10.1016/j.compbiomed.2020.103623

Corti, A., Colombo, M., Migliavacca, F., Rodriguez Matas, J.F., Casarin, S., Chiastra, C., 2021. Multiscale computational modeling of vascular adaptation: A systems biology approach using agent-based models. *Frontiers in Bioengineering and Biotechnology* 9, 744560. https://doi.org/10.3389/fbioe.2021.744560

Corti, A., Colombo, M., Rozowsky, J.M., Casarin, S., He, Y., Carbonaro, D., Migliavacca, F., Rodriguez Matas, J.F., Berceli, S.A., Chiastra, C., 2022. A predictive multiscale model of in-stent restenosis in femoral arteries: linking hemodynamics and gene expression with an agent-based model of cellular dynamics. *Journal of The Royal Society Interface* 20210871. https://doi.org/https://doi.org/10.1098/rsif.2021.0871

Criqui, M.H., Matsushita, K., Aboyans, V., Hess, C.N., Hicks, C.W., Kwan, T.W., McDermott, M.M., Misra, S., Ujueta, F., 2021. Lower Extremity Peripheral Artery Disease: Contemporary Epidemiology, Management Gaps, and Future Directions: A Scientific Statement From the American Heart Association. *Circulation* 144, e171–e191. https://doi.org/10.1161/CIR.0000000000001005

Cunnane, E.M., Mulvihill, J.J.E., Barrett, H.E., Healy, D.A., Kavanagh, E.G., Walsh, S.R., Walsh,

M.T., 2015. Mechanical, biological and structural characterization of human atherosclerotic femoral plaque tissue. *Acta Biomaterialia* 11, 295–303. https://doi.org/10.1016/j.actbio.2014.09.024

Edelman, E.R., Rogers, C., 1998. Pathobiologic responses to stenting. *The American journal of cardiology* 81, 4E-6E. https://doi.org/10.1016/s0002-9149(98)00189-1

Eslami, P., Tran, J., Jin, Z., Karady, J., Sotoodeh, R., Lu, M.T., Hoffmann, U., Marsden, A., 2020. Effect of Wall Elasticity on Hemodynamics and Wall Shear Stress in Patient-Specific Simulations in the Coronary Arteries. *Journal of biomechanical engineering* 142, 245031–2450310. https://doi.org/10.1115/1.4043722

Fok, P.-W., 2016. Multi-Layer Mechanical Model of Glagov Remodeling in Coronary Arteries: Differences between In-Vivo and Ex-Vivo Measurements. *PloS one* 11, e0159304. https://doi.org/10.1371/journal.pone.0159304

Glagov, S., Weisenberg, E., Zarins, C.K., Stankunavicius, R., Kolettis, G.J., 1987. Compensatory Enlargement of Human Atherosclerotic Coronary Arteries. *New England Journal of Medicine* 316, 1371–1375. https://doi.org/10.1056/NEJM198705283162204

Gökgöl, C., Diehm, N., Büchler, P., 2017. Numerical Modeling of Nitinol Stent Oversizing in Arteries with Clinically Relevant Levels of Peripheral Arterial Disease: The Influence of Plaque Type on the Outcomes of Endovascular Therapy. *Annals of Biomedical Engineering* 45, 1420–1433. https://doi.org/10.1007/s10439-017-1803-y

Grundeken, M.J., Chiastra, C., Wu, W., Wykrzykowska, J.J., De Winter, R.J., Dubini, G., Migliavacca, F., 2018. Differences in rotational positioning and subsequent distal main branch rewiring of the Tryton stent: An optical coherence tomography and computational study. *Catheterization and cardiovascular interventions : official journal of the Society for Cardiac Angiography & Interventions* 92, 897–906. https://doi.org/10.1002/ccd.27567

Hafner, N.M., Womack, C.J., Luden, N.D., Todd, M.K., 2016. Arterial adaptations to training among first time marathoners. *Cardiovascular Ultrasound* 14, 1–9. https://doi.org/10.1186/s12947-

016-0063-6

Harrison, D.G., Widder, J., Grumbach, I., Chen, W., Weber, M., Searles, C., 2006. Endothelial mechanotransduction, nitric oxide and vascular inflammation. *Journal of internal medicine* 259, 351–363. https://doi.org/10.1111/j.1365-2796.2006.01621.x

Holland, C.K., Brown, J.M., Scoutt, L.M., Taylor, K.J., 1998. Lower extremity volumetric arterial blood flow in normal subjects. *Ultrasound in medicine & biology* 24, 1079–1086. https://doi.org/10.1016/s0301-5629(98)00103-3

Hoogendoorn, A., Kok, A.M., Hartman, E.M.J., de Nisco, G., Casadonte, L., Chiastra, C., Coenen, A., Korteland, S.A., Van der Heiden, K., Gijsen, F.J.H., Duncker, D.J., van der Steen, A.F.W., Wentzel, J.J., 2020. Multidirectional wall shear stress promotes advanced coronary plaque development: comparing five shear stress metrics. *Cardiovascular research* 116, 1136–1146. https://doi.org/10.1093/cvr/cvz212

Iannaccone, F., Chiastra, C., Karanasos, A., Migliavacca, F., Gijsen, F.J.H., Segers, P., Mortier, P., Verhegghe, B., Dubini, G., De Beule, M., Regar, E., Wentzel, J.J., 2017. Impact of plaque type and side branch geometry on side branch compromise after provisional stent implantation: A simulation study. *EuroIntervention* 13, e236–e245. https://doi.org/10.4244/EIJ-D-16-00498

Jiang, Z., Wu, L., Miller, B.L., Goldman, D.R., Fernandez, C.M., Abouhamze, Z.S., Ozaki, C.K., Berceli, S.A., 2004. A novel vein graft model: adaptation to differential flow environments. *American journal of physiology. Heart and circulatory physiology* 286, H240-5. https://doi.org/10.1152/ajpheart.00760.2003

Kamenskiy, A. V, Pipinos, I.I., Dzenis, Y.A., Phillips, N.Y., Desyatova, A.S., Kitson, J., Bowen, R., MacTaggart, J.N., 2015. Effects of age on the physiological and mechanical characteristics of human femoropopliteal arteries. *Acta biomaterialia* 11, 304–313. https://doi.org/10.1016/j.actbio.2014.09.050

Kasapis, C., Gurm, H.S., 2010. Current approach to the diagnosis and treatment of femoral-popliteal arterial disease. A systematic review. *Current Cardiology Reviews* 5, 296–311.

https://doi.org/10.2174/157340309789317823

Katsanos, K., Tepe, G., Tsetis, D., Fanelli, F., 2014. Standards of practice for superficial femoral and popliteal artery angioplasty and stenting. *CardioVascular and Interventional Radiology* 37, 592–603. https://doi.org/10.1007/s00270-014-0876-3

Kearney, M., Pieczek, A., Haley, L., Losordo, D.W., Andres, V., Schainfeld, R., Rosenfield, K., Isner, J.M., 1997. Histopathology of in-stent restenosis in patients with peripheral artery disease. *Circulation* 95, 1998–2002. https://doi.org/10.1161/01.CIR.95.8.1998

Kim, Y.-H., Kim, J.-E., Ito, Y., Shih, A.M., Brott, B., Anayiotos, A., 2008. Hemodynamic Analysis of a Compliant Femoral Artery Bifurcation Model using a Fluid Structure Interaction Framework. *Annals of Biomedical Engineering* 36, 1753–1763. https://doi.org/10.1007/s10439-008-9558-0

Klein, W.M., Bartels, L.W., Bax, L., Van der Graaf, Y., Mali, W.P.T.M., 2003. Magnetic resonance imaging measurement of blood volume flow in peripheral arteries in healthy subjects. *Journal of Vascular Surgery* 38, 1060–1066. https://doi.org/10.1016/S0741-5214(03)00706-7

Koskinas, K.C., Chatzizisis, Y.S., Antoniadis, A.P., Giannoglou, G.D., 2012. Role of endothelial shear stress in stent restenosis and thrombosis: Pathophysiologic mechanisms and implications for clinical translation. *Journal of the American College of Cardiology* 59, 1337–1349. https://doi.org/10.1016/j.jacc.2011.10.903

Li, S., Lei, L., Hu, Y., Zhang, Y., Zhao, S., Zhang, J., 2019. A fully coupled framework for in silico investigation of in-stent restenosis. *Computer Methods in Biomechanics and Biomedical Engineering* 22, 217–228. https://doi.org/10.1080/10255842.2018.1545017

Liang, H.-L., 2020. Doppler Flow Measurement of Lower Extremity Arteries Adjusted by Pulsatility Index. *AJR. American journal of roentgenology* 214, 10–17. https://doi.org/10.2214/AJR.19.21280

Loree, H.M., Grodzinsky, A.J., Park, S.Y., Gibson, L.J., Lee, R.T., 1994. Static circumferential tangential modulus of human atherosclerotic tissue. *Journal of biomechanics* 27, 195–204.

https://doi.org/10.1016/0021-9290(94)90209-7

Marx, S.O., Totary-Jain, H., Marks, A.R., 2011. Vascular smooth muscle cell proliferation in restenosis. *Circulation: Cardiovascular Interventions* 4, 104–111. https://doi.org/10.1161/CIRCINTERVENTIONS.110.957332

Nikishova, A., Veen, L., Zun, P., Hoekstra, A.G., 2019. Semi-intrusive multiscale metamodelling uncertainty quantification with application to a model of in-stent restenosis. *Philosophical Transactions of the Royal Society A: Mathematical, Physical and Engineering Sciences* 377, 20180154. https://doi.org/10.1098/rsta.2018.0154

Nolan, D.R., Lally, C., 2018. An investigation of damage mechanisms in mechanobiological models of in-stent restenosis. *Journal of Computational Science* 24, 132–142. https://doi.org/10.1016/j.jocs.2017.04.009

Ouzounian, M., Lee, D.S., Gramolini, A.O., Emili, A., Fukuoka, M., Liu, P.P., 2007. Predict, prevent and personalize: Genomic and proteomic approaches to cardiovascular medicine. *The Canadian journal of cardiology* 23 Suppl A, 28A-33A. https://doi.org/10.1016/s0828-282x(07)71003-6

Parmar, J.H., Aslam, M., Standfield, N.J., 2009. Percutaneous transluminal angioplasty of lower limb arteries causes a systemic inflammatory response. *Annals of vascular surgery* 23, 569–576. https://doi.org/10.1016/j.avsg.2009.02.004

Prendergast, P.J., Lally, C., Daly, S., Reid, A.J., Lee, T.C., Quinn, D., Dolan, F., 2003. Analysis of prolapse in cardiovascular stents: a constitutive equation for vascular tissue and finite-element modelling. *Journal of biomechanical engineering* 125, 692–699. https://doi.org/10.1115/1.1613674

Ren, J., Zhou, T., Pilli, V.S.S., Phan, N., Wang, Q., Gupta, K., Liu, Z., Sheibani, N., Liu, B., 2019. Novel Paracrine Functions of Smooth Muscle Cells in Supporting Endothelial Regeneration Following Arterial Injury. *Circulation research* 124, 1253–1265. https://doi.org/10.1161/CIRCRESAHA.118.314567

Rodríguez, J.F., Cacho, F., Bea, J.A., Doblaré, M., 2006. A stochastic-structurally based three

dimensional finite-strain damage model for fibrous soft tissue. *Journal of the Mechanics and Physics of Solids* 54, 864–886. https://doi.org/10.1016/j.jmps.2005.10.005

Schillinger, M., Minar, E., 2005. Restenosis after percutaneous angioplasty: the role of vascular inflammation. *Vascular health and risk management* 1, 73–78. https://doi.org/10.2147/vhrm.1.1.73.58932

Sierra, M., Miana-Mena, F.J., Calvo, B., Muñoz, M.J., Rodríguez, J.F., Grasa, J., 2015. On Using Model Populations to Determine Mechanical Properties of Skeletal Muscle. Application to Concentric Contraction Simulation. *Annals of biomedical engineering* 43, 2444–2455. https://doi.org/10.1007/s10439-015-1279-6

Sindram, D., Martin, K., Meadows, J.P., Prabhu, A.S., Heath, J.J., McKillop, I.H., Iannitti, D.A., 2011. Collagen–elastin ratio predicts burst pressure of arterial seals created using a bipolar vessel sealing device in a porcine model. *Surgical Endoscopy* 25, 2604–2612. https://doi.org/10.1007/s00464-011-1606-4

Smith, M., 2009. ABAQUS/Standard User's Manual. Dassault Systèmes Simulia Corp, Providence, RI, USA.

Sokolis, D.P., 2008. Passive mechanical properties and constitutive modeling of blood vessels in relation to microstructure. *Medical & Biological Engineering & Computing* 46, 1187–1199. https://doi.org/10.1007/s11517-008-0362-7

Stefano, G.T., Mehanna, E., Parikh, S.A., 2013. Imaging a spiral dissection of the superficial femoral artery in high resolution with optical coherence tomography-seeing is believing. *Catheterization and cardiovascular interventions : official journal of the Society for Cardiac Angiography & Interventions* 81, 568–572. https://doi.org/10.1002/ccd.24292

Strauss, B.H., Umans, V.A., van Suylen, R.J., de Feyter, P.J., Marco, J., Robertson, G.C., Renkin, J., Heyndrickx, G., Vuzevski, V.D., Bosman, F.T., Serruys, P.W., 1992. Directional atherectomy for treatment of restenosis within coronary stents: Clinical, angiographic and histologic results. *Journal of the American College of Cardiology* 20, 1465–1473. https://doi.org/10.1016/0735-

1097(92)90438-S

Tahir, H., Bona-Casas, C., Hoekstra, A.G., 2013. Modelling the effect of a functional endothelium on the development of in-stent restenosis. *PLoS ONE* 8, e66138. https://doi.org/10.1371/journal.pone.0066138

Tahir, H., Bona-Casas, C., Narracott, A.J., Iqbal, J., Gunn, J., Lawford, P., Hoekstra, A.G., 2014. Endothelial repair process and its relevance to longitudinal neointimal tissue patterns: comparing histology with in silico modelling. *Journal of The Royal Society Interface* 11, 20140022. https://doi.org/10.1098/rsif.2014.0022

Tahir, H., Hoekstra, A.G., Lorenz, E., Lawford, P. V., Hose, D.R., Gunn, J., Evans, D.J.W., 2011. Multi-scale simulations of the dynamics of in-stent restenosis: impact of stent deployment and design. *Interface Focus* 1, 365–373. https://doi.org/10.1098/rsfs.2010.0024

Tahir, H., Niculescu, I., Bona-Casas, C., Merks, R.M.H., Hoekstra, A.G., 2015. An in silico study on the role of smooth muscle cell migration in neointimal formation after coronary stenting. *Journal of The Royal Society Interface* 12, 20150358. https://doi.org/10.1098/rsif.2015.0358

Tepe, G., Laird, J., Schneider, P., Brodmann, M., Krishnan, P., Micari, A., Metzger, C., Scheinert, D., Zeller, T., Cohen, D.J., Snead, D.B., Alexander, B., Landini, M., Jaff, M.R., 2015. Drug-coated balloon versus standard percutaneous transluminal angioplasty for the treatment of superficial femoral and popliteal peripheral artery disease: 12-month results from the IN.PACT SFA randomized trial. *Circulation* 131, 495–502. https://doi.org/10.1161/CIRCULATIONAHA.114.011004

Toutouzas, K., Colombo, A., Stefanadis, C., 2004. Inflammation and restenosis after percutaneous coronary interventions. *European heart journal* 25, 1679–1687. https://doi.org/10.1016/j.ehj.2004.06.011

Vermeulen, E.G.J., Niessen, H.W.M., Bogels, M., Stehouwer, C.D.A., Rauwerda, J.A., van Hinsbergh, V.W.M., 2001. Decreased Smooth Muscle Cell/Extracellular Matrix Ratio of Media of Femoral Artery in Patients With Atherosclerosis and Hyperhomocysteinemia.

51

Arteriosclerosis, Thrombosis, and Vascular Biology 21, 573–577. https://doi.org/10.1161/01.ATV.21.4.573

Wong, M., Edelstein, J., Wollman, J., Bond, M.G., 1993. Ultrasonic-pathological comparison of the human arterial wall. Verification of intima-media thickness. *Arteriosclerosis and Thrombosis: A Journal of Vascular Biology* 13, 482–486. https://doi.org/10.1161/01.ATV.13.4.482

Wood, N.B., Zhao, S.Z., Zambanini, A., Jackson, M., Gedroyc, W., Thom, S.A., Hughes, A.D., Xu, X.Y., 2006. Curvature and tortuosity of the superficial femoral artery: a possible risk factor for peripheral arterial disease. *Journal of applied physiology (Bethesda, Md. : 1985)* 101, 1412–1418. https://doi.org/10.1152/japplphysiol.00051.2006

Wyttenbach, R., Gallino, A., Alerci, M., Mahler, F., Cozzi, L., Di Valentino, M., Badimon, J.J., Fuster, V., Corti, R., 2004. Effects of percutaneous transluminal angioplasty and endovascular brachytherapy on vascular remodeling of human femoropopliteal artery by noninvasive magnetic resonance imaging. *Circulation* 110, 1156–1161. https://doi.org/10.1161/01.CIR.0000140672.70862.5B

Ye, D., Nikishova, A., Veen, L., Zun, P., Hoekstra, A.G., 2021. Non-intrusive and semi-intrusive uncertainty quantification of a multiscale in-stent restenosis model. *Reliability Engineering & System Safety* 214, 107734. https://doi.org/https://doi.org/10.1016/j.ress.2021.107734

Zahedmanesh, H., Van Oosterwyck, H., Lally, C., 2014. A multi-scale mechanobiological model of in-stent restenosis: deciphering the role of matrix metalloproteinase and extracellular matrix changes. *Computer Methods in Biomechanics and Biomedical Engineering* 17, 813–828. https://doi.org/10.1080/10255842.2012.716830

Zun, P.S., Anikina, T., Svitenkov, A., Hoekstra, A.G., 2017. A comparison of fully-coupled 3D in-stent restenosis simulations to in-vivo data. *Frontiers in Physiology* 8, 1–12. https://doi.org/10.3389/fphys.2017.00284

Zun, P.S., Narracott, A.J., Chiastra, C., Gunn, J., Hoekstra, A.G., 2019. Location-specific comparison between a 3D in-stent restenosis model and micro-CT and histology data from porcine in vivo

experiments. *Cardiovascular Engineering and Technology* 10, 568–582. https://doi.org/10.1007/s13239-019-00431-4